DISCLAIMER

GTI ENERGY

solutions that transform

Final Scientific/Technical Report

DOE Award No. DE-FE0032215 (GTI 23379)

Transformational Nano-confined Ionic Liquid Membrane for Greater than or Equal to 97 Percent Carbon Dioxide Capture from Natural Gas Combined Cycle Flue Gas

Reporting Period:
March 1, 2023 – May 31, 2025

Report Issued:
September 30, 2025

Principal Authors:
Shiguang Li, Weiwei Xu, Qiaobei Dong, Howard Meyer
GTI Energy

Miao Yu, Fan Wang, Dinesh Behera, Preety Kumari, Chiamaka Chukwujama
The State University of New York at Buffalo

Technical Contact:
Dr. Shiguang Li (Principal Investigator)
(847) 544-3478
SLi@gti.energy

DOE Project Manager:
Mr. Andrew O'Palko, Project Manager
National Energy Technology Laboratory (NETL)
(304) 285-4715
andrew.opalko@netl.doe.gov

Name and Address of Submitting Organizations:
GTI Energy
1700 S. Mt. Prospect Rd.
Des Plaines, IL 60018

Disclaimer

This presentation was prepared by GTI Energy as an account of work sponsored by an agency of the United States Government.

Neither GTI Energy, the partners of GTI Energy, the Sponsor(s), nor any person acting on behalf of any of them:

a. Makes any warranty or representation, express or implied with respect to the accuracy, completeness, or usefulness of the information contained in this report, or that the use of any information, apparatus, method, or process disclosed in this report may not infringe privately-owned rights. Inasmuch as this project is experimental in nature, the technical information, results, or conclusions cannot be predicted. Conclusions and analysis of results by GTI Energy represent GTI Energy's opinion based on inferences from measurements and empirical relationships, which inferences and assumptions are not infallible, and with respect to which competent specialists may differ.

b. Assumes any liability with respect to the use of, or for any and all damages resulting from the use of, any information, apparatus, method, or process disclosed in this report; any other use of, or reliance on, this report by any third party is at the third party's sole risk.

c. The results within this report relate only to the items tested.

Abstract

A transformational process based on nano-confined ionic liquid (NCIL) membranes was developed for capturing ≥97% CO_2 from natural gas combined cycle (NCCC) flue gas. The NCIL membranes were prepared by loading amino acid ionic liquid into a framework composed of single-walled carbon nanotube mesh filled with graphene oxide quantum dots. The membranes exhibited CO_2 permeance as high as 2,000 GPU with a CO_2/N_2 selectivity of 2,300 for a typical NGCC flue gas composition. When H_2O vapor sweep was applied in the permeate side, 96.6% CO_2 dry-basis purity and 97.6% CO_2 capture rate were achieved for a simulated NGCC flue gas with single stage.

In the process design, a highly H_2O-selective membrane would be needed to recover majority of the H_2O vapor, and the recovered H_2O vapor could be recycled to the permeate side of the NCIL membrane. Sulfonated poly(ether ether ketone) membranes were successfully developed for this purpose. These membranes exhibited H_2O permeance great than 11,000 GPU and H_2O/CO_2 selectivity greater than 1,000 at 70ºC for a feed mixture consisting of 14.5 vol% H_2O and balanced CO_2.

A standalone membrane model using MATLAB platform was developed for process simulation. The model was validated with experimental data. Techno-economic analysis based on the testing data collected during the current program suggests this transformational membrane process can achieve 97% CO_2 capture efficiency with a cost of $47.8/tonne of CO_2, which is a 21% reduction versus DOE's reference case B31B.97.

Acknowledgments

We gratefully acknowledge financial support by the U.S. Department of Energy (Contract Number DE-FE0032215).

We thank DOE Project Management Team Andrew O'Palko, Michael Fasouletos, Timothy Fout and Dan Hancu for their technical support.

Table of Contents

Executive Summary

This report summarizes the carbon capture research and development conducted by GTI Energy and The State University of New York at Buffalo for award "DE-FE0032215: Transformational Nano-confined Ionic Liquid Membrane for Greater than or Equal to 97 Percent Carbon Dioxide Capture from Natural Gas Combined Cycle Flue Gas" sponsored by the U.S. Department of Energy (DOE). The objectives of this project were 1) to develop a transformational membrane technology capturing ≥97% CO_2 from natural gas combined cycle (NGCC) flue gas, and 2) to demonstrate significant progress towards a 40% reduction in the cost of CO_2 capture versus a reference NGCC power plant for the same carbon capture efficiency.

A transformational process based on nano-confined ionic liquid (NCIL) membranes was developed for capturing ≥97% CO_2 from a NGCC flue gas. The NCIL membranes were prepared by loading amino acid ionic liquid into a framework composed of single-walled carbon nanotube (SWCNT) mesh filled with graphene oxide quantum dots (GOQDs). The ultra-permeable SWCNT nanoconfined structure was optimized to provide minimum gas transport resistance and maximum confinement for stabilization of the ionic liquid. The investigation of transport resistance and breakthrough pressure demonstrated superiority of the SWCNT network, which combines high ε/τ factor with strong confinement force. Specifically, continuous pressurization test verified the effectiveness of nano-confinement of the SWCNT mesh even under a pressure difference (between feed and permeate) of 30 bar. The nano-confined space between SWCNTs, combined with nanometer-sized GOQDs with rich oxygen-containing functional groups, stabilizes the amino acid ionic liquids with amine groups during membrane operations.

The NCIL membranes exhibited CO_2 permeance as high as 2,000 GPU with a CO_2/N_2 selectivity of 2,300 for a typical NGCC flue gas composition. To increase driving force for the permeation of CO_2, water vapor sweep was applied in the permeate side of the membrane. Both co-current and counter-current flow modes were investigated. In a test with counter-current flow mode, 96.6% CO_2 dry-basis purity and 97.6% CO_2 capture rate were achieved with a single membrane stage for a simulated NGCC flue gas.

An innovative water-vapor sweep and recycling process was designed to use the high-selectivity NCIL membrane to achieve ≥95% CO_2 purity and ≥97% CO_2 capture efficiency by a single membrane stage for a typical NGCC flue gas feed (~4 vol% CO_2). In this process design, a highly H_2O-selective membrane would be needed to recover majority of the H_2O vapor, and the recovered H_2O vapor could be recycled to the permeate side of the NCIL membrane. To meet this requirement, highly H_2O-selective sulfonated poly(ether ether ketone) (SPEEK) membranes were developed. These membranes exhibited H_2O permeance great than 11,000 GPU and H_2O/CO_2 selectivity greater than 1,000 at 70ºC for a feed mixture containing 14.5 vol% H_2O and balanced CO_2. The membranes also showed good stability during continuous operations.

A standalone membrane model using MATLAB platform was developed to simulate the permeation of a multi-component gas mixture, containing N_2, CO_2, and H_2O, through a membrane module. In this model, the inputs include feed gas composition, feed gas flow rate, sweep gas composition, sweep gas flow rate, pressures of the feed and sweep gas streams, and membrane area. The model outputs are the gas compositions and flow rates of the retentate and permeate sides. The model was validated with experimental data.

The membrane model was then integrated with Aspen Plus and Excel for process design and simulation. In a typical process design, the feed conditions are defined within Aspen Plus, along with the membrane block specifications. These parameters were then exported from Aspen Plus to Excel. After necessary unit conversions and reformatting of the data arrays, the Excel provided input for the membrane model in the MATLAB. The results from the MATLAB were then returned to Excel, which provided input back to the Aspen Plus, enabling process design and simulation. This integrated platform was used to perform process design for a typical NGCC power plant (~650 MWe net power). For 97% CO_2 capture, a membrane area of approximately 1.5×10^6 m^2 would be needed.

Techno-economic analysis (TEA) based on testing data collected was conducted for a 97% CO_2 removal system utilizing the NCIL membrane-based process. The design basis followed the guidance provided by the DOE National Energy Technology Laboratory's "Rev 4a Baseline Report". In the baseline report, Case B31A operates without CO_2 capture, while Case B31B.97 achieves 97% CO_2 capture by using Shell CANSOLV® solvent technology. The TEA suggests that the NCIL membrane-based process can achieve 97% CO_2 capture efficiency with a cost of $47.8/tonne of CO_2, which is a 21% cost reduction versus DOE's reference case B31B.97.

1. Introduction

1.1. Nano-confined Ionic Liquid Membranes versus State-of-the-art Membranes for Post-combustion CO_2 Capture

Thirteen membrane-related projects for post-combustion CO_2 capture are listed in DOE's Carbon Capture Program portfolio.[1] The most representative membranes with high CO_2/N_2 separation performance are summarized in Table 1.

Table 1. *Representative membrane technologies funded in DOE's Carbon Capture Program portfolio*.

Organization	Material	Feed	CO_2 permeance, GPU	CO_2/N_2 selectivity
MTR	Polaris™	10-40% CO_2	3,000 (Gen-3)	50
OSU	Amine-polymer	13.17% CO_2	3,500	170
GTI	Graphene oxide-based	4-13% CO_2	1,020	680
Air Liquide	Polyimide-based	13.17% CO_2	Not available	50
Luna Innovations	Molten electrolyte	20% CO_2	800	999

The project team has developed a transformational nano-confined ionic liquid (NCIL) membrane by loading amino acid ionic liquid (AAIL) into a framework composed of single-walled carbon nanotube (SWCNT) mesh filled with graphene oxide quantum dots (GOQDs) (Figure 1). The nano-confined space between SWCNTs, combined with nanometer-sized GOQDs with rich oxygen-containing functional groups,[2–6] stabilizes the amino acid ILs with amine groups during membrane operations. The polymeric porous support with high gas permeance provides the mechanical strength necessary for operation under pressure-driven permeation.

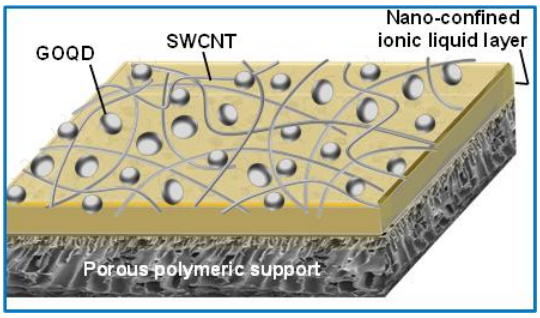

Figure 1. *Schematic of the proposed NCIL membrane.*

The NCIL-selective layer with the SWCNT/GOQD framework, typically 300–500 nm thick, separates CO_2 from N_2 with high selectivity. As shown in Figure 2, on the feed side with higher partial pressure, CO_2 molecules first react with the anion of amino acid IL and water to form CO_2 complexes. Then, the CO_2-complexes diffuse through the membrane and decompose to release the CO_2 molecules via the reverse reaction at the low-pressure permeate side. The regenerated amino acid IL mobile carriers diffuse back to the feed side and get ready for bonding with CO_2 molecules on the feed side. This is called a "facilitated transport mechanism".[7,8] The amino acid IL mobile carriers are nonvolatile and will stay in the membrane to facilitate long-term and fast CO_2 transport.

The permeation of N_2 is extremely slow because of its chemical inertness to the carriers. Moreover, the enhanced viscosity of NCIL, resulting from the nano-confined space in SWCNT mesh and favorable interactions between rich functional groups on GOQDs and ILs, significantly inhibits N_2 permeation. This results in a super high CO_2/N_2 selectivity, which is 2-3 orders of magnitude higher than those shown by membranes relying on size or condensability discrimination through the solution-diffusion mechanism.

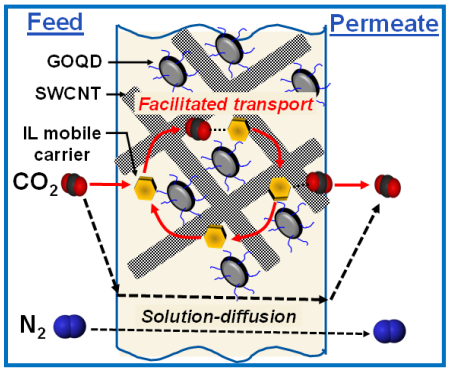

***Figure 2**. Schematic of transport mechanism.*

1.2. Integration of NCIL Membrane with a Highly H_2O-selective Membrane

An innovative water-vapor sweep and recycling process was designed to use the high-selectivity membrane to achieve ≥95% CO_2 purity and ≥97% CO_2 capture efficiency by a single membrane stage for a typical NGCC flue gas feed (~4 vol% CO_2). A highly H_2O-selective membrane was designed to recover majority of the H_2O vapor, and the recovered H_2O vapor was recycled to the permeate side of the NCIL membrane.

Many polymeric membrane materials, including sulfonated poly(ether ether ketone) (SPEEK), polydimethylsiloxane, sulfonated polyethersulfone, and cellulose acetate, have been investigated for water vapor removal from gas streams.[9–13] The H_2O/N_2 selectivity verse H_2O vapor permeability of these polymeric membranes have been summarized in the literature.[14,15] As shown in Figure 3, very promising materials are located in the upper right corner and indicated by the shaded area.

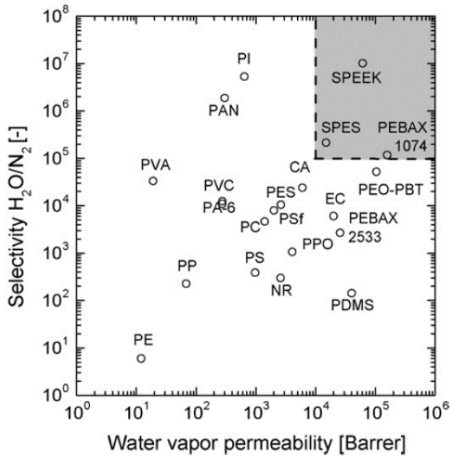

***Figure 3**. Water vapor permeability vs. water vapor/N_2 selectivity at 30°C.*

Among these promising materials, SPEEK and PEBAX 1074 have been made into membranes by casting or dip coating and studied for flue gas dehydration at different temperatures.[16] The H_2O/CO_2 selectivities were reported to be 1,000-5,000 for the SPEEK and 100-150 for the PEBAX 1074 at 70°C. Therefore, the SPEEK membrane was more promising than PEBAX 1074 for the highly selective recovery of H_2O vapor from CO_2-containg streams. It was thus identified was the focused material for development in the current DOE project.

1.3. Project Objectives and Team

The objectives of this project were: 1) to develop a transformational membrane technology capturing ≥97% CO_2 from a natural gas combined cycle (NGCC) flue gas, and 2) to demonstrate significant progress towards a 40% reduction in the cost of CO_2 capture versus a reference NGCC power plant for the same carbon capture efficiency.

The project team included GTI Energy (GTI) and the University at Buffalo (UB). The proposed program uses each Team Member's unique expertise (GTI: membrane process design and UB: membrane development) that is critical to conducting the studies to advance the technology from TRL 2 to TRL 3.

2. Experimental Methods, Assumptions, and Procedures

2.1. Preparation of NCIL Membranes

2.1.1. Coating Solution Preparation

Single-wall carbon nanotube powder (SWCNT, OD< 3 nm, length 5 μm, purity>85%, TCI), sodium dodecyl benzenesulfonate (SDBS, 99%, TCI), 1-ethyl-3-methylimidazolium glycine ([Emim][Gly], >98%, BLD pharm) were used as received. Polyethersulfone substrates (PES, 30/100/450 nm, 51 mm diameter) were purchased from Steritech Corporation. Polyethersulfone hollow fiber substrates (PES, 75 cm^2, 300 kDa molecular weight cut-off [MWCO], 1 mm inner diameter) were purchased from Repligen Corporation. Polyethylene glycol (PEGs, molecular weight: 600 Da, 2 kDa and 10 kDa, 35 kDa) and Polyethylene oxide (PEOs, molecular weight: 100 kDa, 300 kDa) were purchased from Sigma-Aldrich. Premixed gas (15% CO_2/85% N_2), pure gas (99.9 mol% N_2, 99.9 mol% CO_2, 99.99 mol% Helium) for membrane permeation measurements were purchased from Airgas.

In a typical synthesis of coating solution, 0.1 mg of CNT powder was added into 1 liter of as-prepared SDBS solution (1 mg SDBS per mL D.I. water) and dispersed via ultra-sonication (Fisher Scientific S450) for 1 h. Next, the CNT dispersion was sonicated and then centrifuged at 10,000 rounds per minute (rpm) for 25 min. The supernatant was collected as final CNT dispersion with CNT concentration of 0.06 mg mL^{-1}. Finally, the CNT dispersion was diluted into D.I. water to make a 1 μg mL^{-1} CNT coating solution.

2.1.2. Flat Sheet NCIL Membrane Fabrication

A controlled volume of the CNT coating solution was vacuum-filtrated onto a flat sheet PES substrate (450 nm pore size) to fabricate the CNT nanomesh. The resulting CNT nanomesh was dried in oven at 70°C for 1 h. Flat-sheet NCIL membranes were prepared using a dip-coating method. The coating solution was prepared by adding controlled amount of IL ([Emim][Gly], 98%) into D.I. water (10 mL). Then, the dip coating solution was stirred for 10 min. The dip-coating procedure was illustrated in Figure 4.

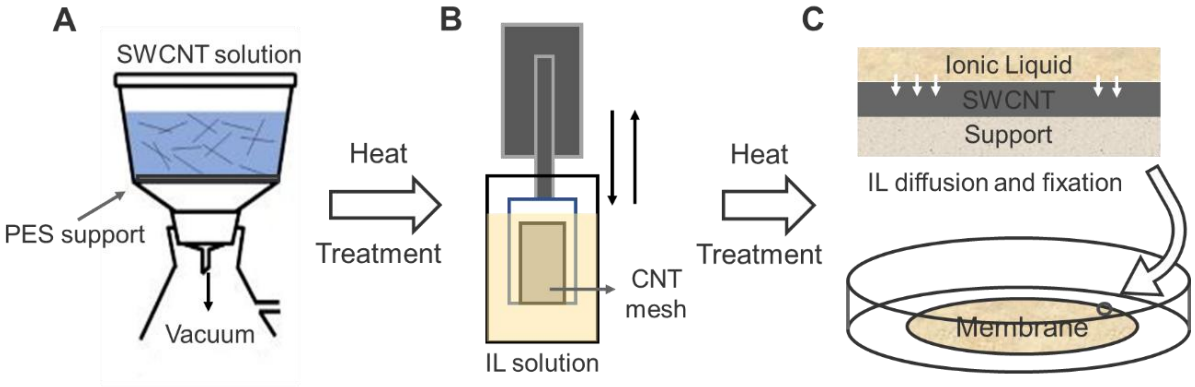

Figure 4. *Schematic of flat sheet NCIL membrane fabrication. (A) Vacuum filtration for CNT mesh coated PES membrane preparation; (B) Dip coating for IL loading onto the CNT mesh; (C) Demonstration of IL impregnation into the CNT mesh for the formation of NCIL membranes.*

As-prepared CNT nanomesh on PES substrate was cut into 2cm × 4cm flat sheet and taped onto a microscopic slide and then fixed onto the rod of dip coater. The moving speed of the dip coater rod was set to be 1×10^{-3} $m\cdot s^{-1}$. During the dip-coating process, the CNT nanomesh was completely immersed in the IL coating solution for 1s and then removed from the solution following the pre-set program. Finally, the NCIL membrane was transferred to a petri dish and dried in oven at 70°C for 1 h.

2.1.3. Fabrication of NCIL Membranes onto Hollow Fiber Substrates

The CNT nanomesh on hollow fiber PES substrate was first prepared using a modified vacuum-assisted coating system as illustrated in Figure 5A. D.I. water was introduced to fill up the PES hollow fiber substrate to remove glycols within the substrate. The pumping rate of the D.I. water was controlled by a syringe pump. Next, the CNT solution was infused into the washed support until the air bubbles inside the fibers were removed. A vacuum pressure of 0.2 bara was sequentially applied in the permeate side of hollow fiber module, and the CNT coating solution started to be pulled into hollow fiber. After completing consumption of the CNT coating solution, vacuum was maintained on the permeate side for another 30 min to remove D.I. water from the module. Finally, the resulting CNT nanomesh supported on the PES hollow fiber substrate was removed from the coating system and dried in an oven at 70°C for overnight.

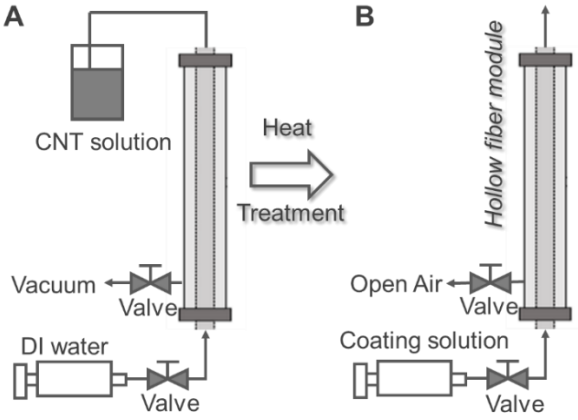

Figure 5. *Fabrication of NCIL membranes onto hollow fiber substrates. (A) Vacuum filtration of CNT onto the inner surface of the PES hollow fiber substate; (B) Dip-coating of IL solution onto the CNT mesh coated PES substrate.*

The NCIL hollow fiber membranes were also prepared via a dip-coating method as shown in Figure 5B. The dip-coating solution was prepared by adding 12 g of [Emim][Gly] into 60 mL D.I. water with stirring for 10 min. At the beginning of the dip-coating process, the amino acid ionic liquid (AAIL) solution was pumped into the CNT nanomesh coated hollow fibers with a controlled pumping rate of 3 mL min^{-1}. After filling-up of the hollow fibers with IL solution, the syringe pump was shut down to allow IL solution to slowly flow out of the hollow fibers by gravity. Finally, the NCIL hollow fiber membrane was removed from the coating system and dried in an oven at 70°C for overnight.

2.2. Preparation of Dehydration Membranes

2.2.1. Synthesis of SPEEK

SPEEK was prepared by sulfonation of PEEK. PEEK is a semi-crystalline polymer purchased from Sigma Aldrich (USA). Its molecular structure is shown in Figure 6.

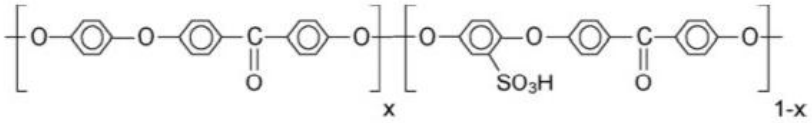

Figure 6*. Molecular structure of SPEEK.*

Sulfonation procedure of PEEK is outlined in Figure 7. Specifically, 60g of PEEK was dried in vacuum oven at 100°C for one week and then dissolved in 1 L of sulfuric acid (95–98 wt%). The solution was vigorously stirred at 25ºC for 120 h. After the completion of reaction, the mixture was precipitated and washed with D.I. water until pH >5. After drying at room temperature, the sulfonated polymer was further dried in vacuum oven at 30°C for another 48 h.

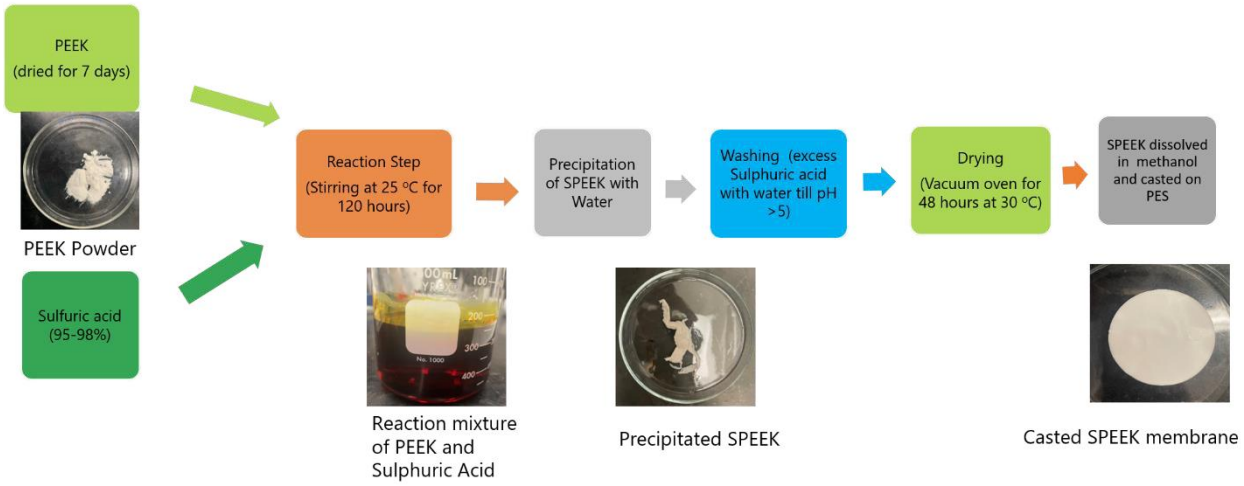

Figure 7. *Methodology employed for synthesis of SPEEK and fabrication of SPPEK membranes.*

2.2.2. Fabrication of SPEEK Membranes

SPEEK membranes were fabricated by using SPEEK/methanol solution with different SPEEK concentrations and different coating methods. The substrates used for membrane coating were PES (pore size: 450 nm) and PEEK (pore size: 20 nm).

2.3. Characterization of Membranes

2.3.1. General Characterization

The surface and cross-sectional morphology of membranes were characterized by Focused

Ion Beam Scanning Electron Microscope (FIB-SEM)-Carl Zeiss AURIGA. Elements distributions of NCIL membranes were analyzed via Energy-Dispersive Spectroscopy (EDS, Hitachi SU70). Fourier-transform Infrared spectroscopy (FTIR, BRUKER VERTEX 70) was performed to investigate the IL incorporation within the NCIL membranes. The NCIL membrane structure and chemical properties were analyzed by X-ray Photoelectron Spectroscopy (XPS, AXIS Ultra DLD, Kratos Analytical). The MWCO of the CNT mesh was characterized by Gel Permeation Chromatography (GPC, Agilent 1260 Infinity II, Column: Agilent OligoPore, PL1113-6520) via applying PEG filtration through CNT/PES membranes as described in the following section.

2.3.2. PEG Rejection and Effective Pore Size Characterization

Effective pore size and pore size distribution of the membranes were determined by the rejection of a series of PEGs/PEOs (10 kDa, 100 kDa, 300 kDa, 1000 kDa, 5000 kDa). The hydrodynamic diameter (d_s) of the PEG molecules was calculated based on Equation 1. Effective pore radius (r_p) was determined by the modified Ferry's equation (Equation 2) for 90% Rejection (R) of PEG,[23] where r_s is the hydrodynamic radius of the PEG/PEO solute:

$$d_s\,(nm) = 0.09 \times MW^{0.44} \tag{1}$$

$$R = 1 - \left(1 - \frac{r_s}{r_p}\right)^2 - \left(1 - \frac{r_s}{r_p}\right)^4 \tag{2}$$

2.3.3. Theoretical Capillary/Breakthrough Pressure Calculation

The theoretical capillary breakthrough pressure of the CNT mesh was calculated to estimate effectiveness of nanoconfinement, following the simplified Young-Laplace equation:[25]

$$Breakthrough\ Pressure = BP = \frac{2\gamma cos\theta}{r_p} \tag{3}$$

Where γ is surface tension of the ionic liquid [Emim][Gly] of 53.5 $mN \cdot m^{-2}$;[26] θ the contact angle between the ionic liquid [Emim][Gly] and the pore surface of 45°; r_p the effective pore radius of the CNT mesh, with minimum value of 10 nm. Given all the parameters mentioned above, the theoretical breakthrough pressure ranges from 25 bar to 152 bar.

2.4. Gas Permeation Measurement for the NCIL Membranes

Single-gas permeation test was conducted by using a sweep system shown in Figure 8. Flat sheet membrane was cut into 2cm × 4cm small piece and put inside of a stainless-steel membrane permeation cell with an effective surface area of 0.23 cm^2. Dry CO_2/N_2 gas mixture was first generated and controlled by mass flow controllers (MFCs, Brooks 5850S). Water vapor was then introduced via a humidifier to the dry CO_2/N_2 gas mixture to make up feed gases with different water vapor compositions. The mass flow controller in the retentate side of membrane was used to adjust the feed pressure by controlling the retentate side gas flow rate. The permeate pressure was controlled by a needle valve, which was located in between the membrane permeate outlet and a vacuum pump. The permeate gas was carried by helium (60 mL min^{-1}) and sent to a gas chromatography (GC7890, Agilent) for gas composition analysis. The permeation temperature was controlled by an air-forced oven.

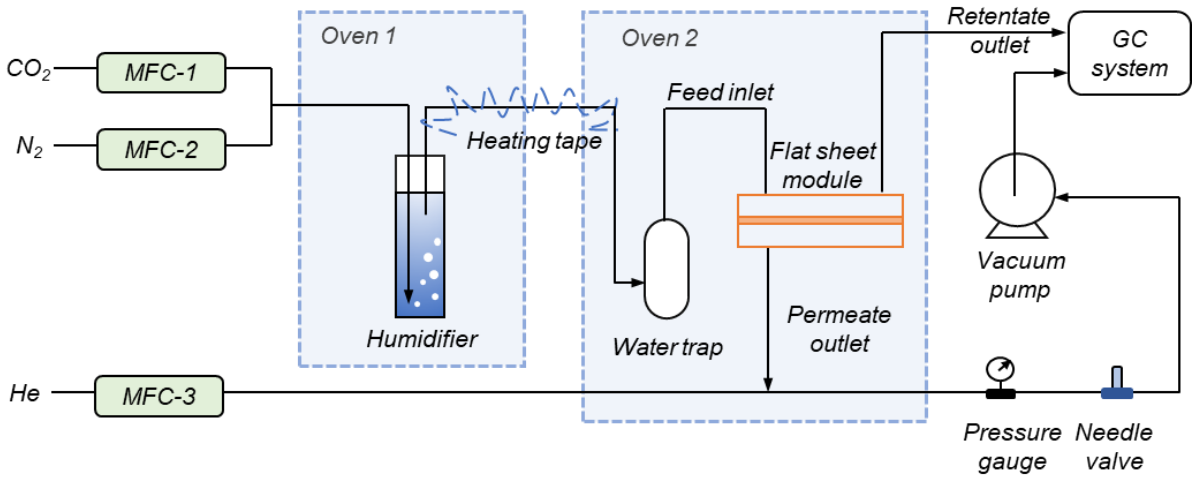

***Figure 8**. Process flow diagram for a gas permeation system used for flat sheet membranes.*

Gas permeance P_i of component i for flat sheet membrane was calculated by:

$$P_i = \frac{J_i}{A \cdot \Delta P_i} \tag{4}$$

$$\Delta P_i = P_{f,i} - P_{p,i} \tag{5}$$

Where A is the effective membrane area, J_i molar flow rate of gas component i through the membrane, ΔP_i partial pressure difference of gas component i between membrane feed side and permeate side. The gas separation selectivity α_{ij} was calculated by:

$$\alpha_{ij} = \frac{P_i}{P_j} \tag{6}$$

For gas mixture permeation measurement of the hollow fiber membranes, the system setup is shown in Figure 9.

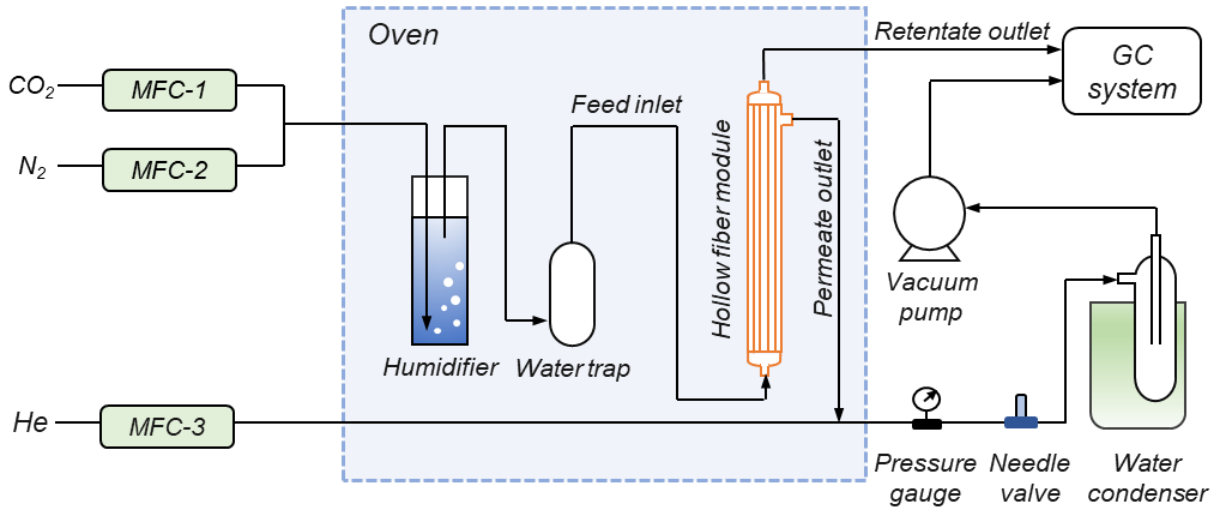

***Figure 9**. Process flow diagram for a gas permeation system used for hollow fiber membranes.*

During a test, a NCIL hollow fiber membrane was placed vertically within an oven. The simulated natural gas flue gas was introduced to the bottom side of the membrane. A water condenser inside a chiller was assembled before a vacuum pump to condense water vapor from the permeate stream. Then, the water vapor-free permeate gas was carried by helium and sent to a gas chromatography (GC7890, Agilent) for gas composition analysis.

The membranes were also tested using a water vapor sweep mode. In that case, as shown in Figure 10, in the left oven, water vapor was introduced to the feed mixture by a humidifier. In the right oven, water vapor was generated by vacuuming the water tank and used as sweeping gas in the permeate side of the membrane. The water vapor flow rate was controlled by adjusting the opening of the needle valve. Both co-current and counter-current flow modes (Figure 11) were tested.

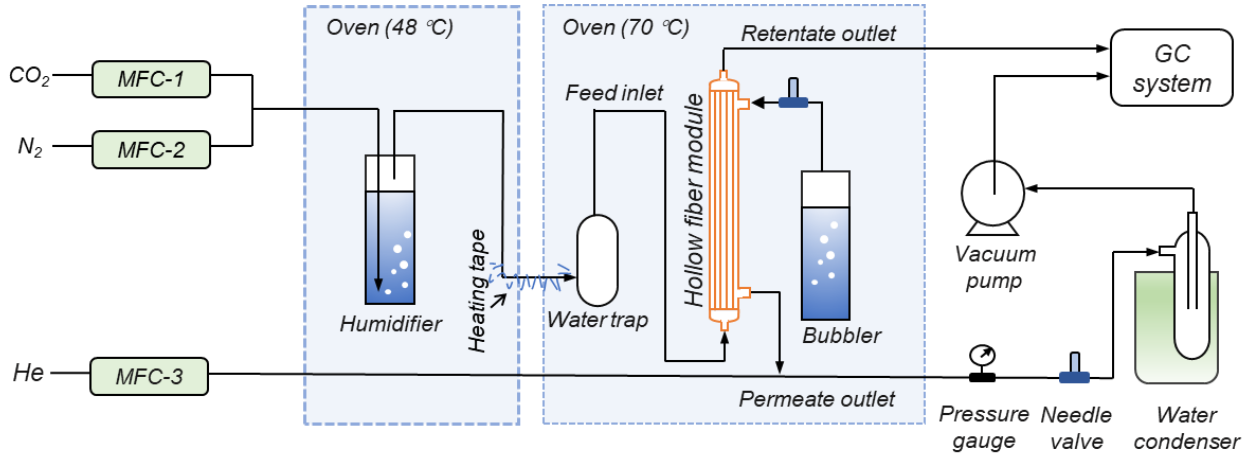

Figure 10. *NCIL hollow fiber membrane testing system using water vapor sweep mode.*

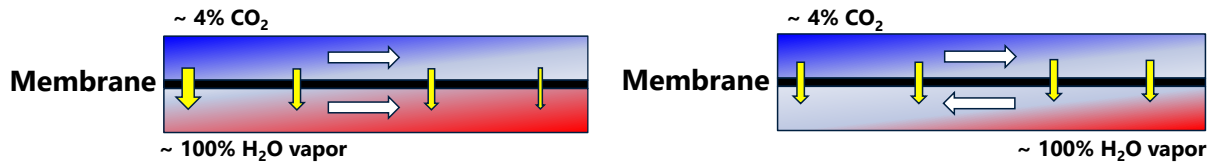

Figure 11. *(A) co-current and (B) counter-current water vapor sweep modes.*

The gas permeance P_i of component i was calculated by:

$$P_i = \frac{J_i}{A \cdot \Delta P_{i,ln}} \tag{7}$$

$$\Delta P_{i,ln} = \left(\frac{(P_{f,i} - P_{p,i}) - (P_{r,i} - P_{p,i})}{ln\,(P_{f,i} - P_{r,i})} \right) - P_{p,i} \tag{8}$$

Where $\Delta P_{i,ln}$ is the log-mean pressure drop through the hollow fiber, simplified model was applied to calculate driving force of species i. $P_{f,i}$, $P_{r,i}$, $P_{p,i}$ represent partial pressure of gas component i

in feed, retentate, permeate side of membrane, respectively. The gas separation selectivity α_{ij} was calculated by:

$$\alpha_{ij} = \frac{P_i}{P_j} \tag{9}$$

The CO_2 capture rate and dry-basis purity of hollow fiber membrane were calculated by:

$$CO_2\ capture\ rate = \frac{F_{p,CO_2}}{F_{f,CO_2}} \times 100\% \tag{10}$$

$$CO_2\ dry\ basis\ purity = \frac{F_{p,CO_2}}{F_{p,CO_2}+F_{p,N_2}} \times 100\% \tag{11}$$

Where F_{p,CO_2}, F_{p,N_2} are the flow rate of CO_2 and N_2 in permeate side of hollow fiber membrane, respectively. F_{f,CO_2} the flow rate of CO_2 in feed side of hollow fiber membrane.

2.5. Gas Permeation Measurement for the Dehydration Membranes

Similar approaches were used for the gas permeation measurement of the dehydration membranes except for the feed gas containing 14.5 vol% CO_2 and balanced water vapor. The testing temperature was 70ºC. Helium was employed in the permeate side of SPEEK membrane as sweeping gas. Small area (~0.25 cm^2) flat sheet SPEEK membranes were used for preliminary testing and screening. The membranes were then scaled up to 10 cm^2, and their gas permeation properties were tested.

2.6. Membrane Modeling and Process Simulation

GTI developed a standalone membrane model using MATLAB platform. A one-dimensional model [17,18] was used to simulate gas permeation of a gas mixture containing N_2, CO_2, and H_2O, through a membrane module. A plug flow was assumed on the feed side with negligible pressure drop, while the permeate side incorporated a counter-current flow pattern with sweep gas (water vapor).

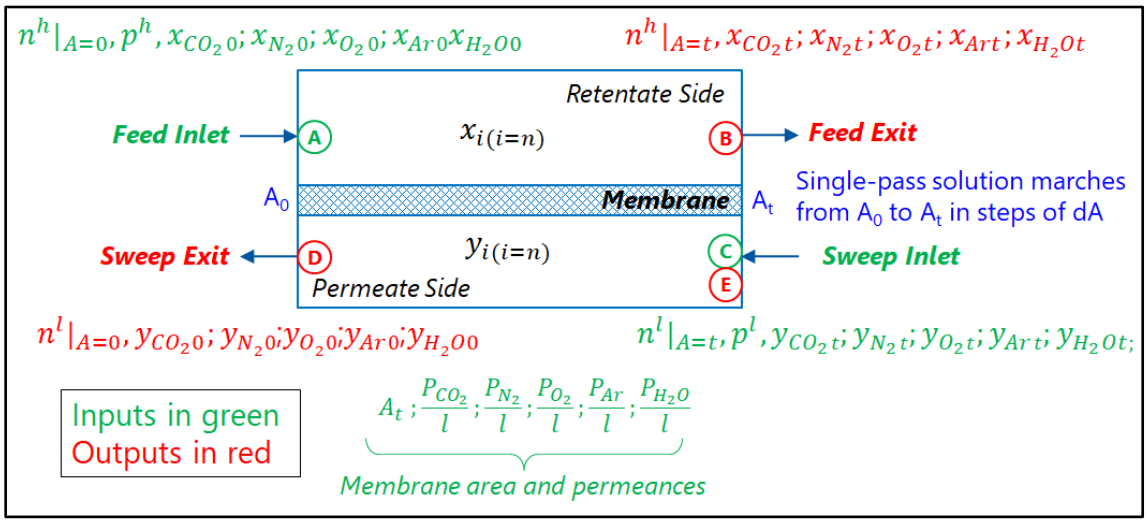

Figure 12. *Membrane model input and output parameters.*

In this membrane model, the inputs include feed gas composition, feed gas flow rate, sweep gas composition, sweep gas flow rate, the pressures of the feed and sweep gas streams, and the membrane area. The model outputs are the gas compositions and flow rates of the retentate and permeate sides. As shown in Figure 12, the inputs and outputs are highlighted in green and red, respectively.

The solution approach can be described by referencing the circled letters (A) through (E) in Figure 12. The single pass solution starts at A_0 and marches left-to-right in increments of dA across the membrane to A_t. However, the sweep exit conditions at (D) are initially unknown, so a guess of flow rate and composition at (D) shall be made to start the area-matching solution. At the conclusion of each single pass, conditions at (B) and (E) are calculated. Composition and flow rates at (E) are compared to known sweep gas inlet conditions of (C). A new guess of sweep exit conditions at (D) are made by a simple error comparison of each parameter (flowrate and mole fractions) multiplied by a convergence factor. Note that this model assumes constant, but different, pressures on both sides of the membrane. A maximum error tolerance is input, and the solution loop proceeds until the sum of the absolute flowrate and mole fraction errors are less than the tolerance, up to a defined maximum iteration limit.

The equations solved by the membrane model are listed in Figure 13.

$$\frac{dn^h}{dA} = -J \qquad \frac{dn^l}{dA} = -J$$

$$\frac{dx_{CO_2}}{dA} = -\frac{1}{n^h}\left[\frac{P_{CO_2}}{l}\left(p^h x_{CO_2} - p^l y_{CO_2}\right) - x_{CO_2} * J\right] \qquad \frac{dy_{CO_2}}{dA} = -\frac{1}{n^l}\left[\frac{P_{CO_2}}{l}\left(p^h x_{CO_2} - p^l y_{CO_2}\right) - y_{CO_2} * J\right]$$

$$\frac{dx_{N_2}}{dA} = -\frac{1}{n^h}\left[\frac{P_{N_2}}{l}\left(p^h x_{N_2} - p^l y_{N_2}\right) - x_{N_2} * J\right] \qquad \frac{dy_{N_2}}{dA} = -\frac{1}{n^l}\left[\frac{P_{N_2}}{l}\left(p^h x_{N_2} - p^l y_{N_2}\right) - y_{N_2} * J\right]$$

$$\frac{dx_{O_2}}{dA} = -\frac{1}{n^h}\left[\frac{P_{O_2}}{l}\left(p^h x_{O_2} - p^l y_{O_2}\right) - x_{O_2} * J\right] \qquad \frac{dy_{O_2}}{dA} = -\frac{1}{n^l}\left[\frac{P_{O_2}}{l}\left(p^h x_{O_2} - p^l y_{O_2}\right) - y_{O_2} * J\right]$$

$$\frac{dx_{Ar}}{dA} = -\frac{1}{n^h}\left[\frac{P_{Ar}}{l}\left(p^h x_{Ar} - p^l y_{Ar}\right) - x_{Ar} * J\right] \qquad \frac{dy_{Ar}}{dA} = -\frac{1}{n^l}\left[\frac{P_{Ar}}{l}\left(p^h x_{Ar} - p^l y_{Ar}\right) - y_{Ar} * J\right]$$

$$\frac{dx_{H_2O}}{dA} = -\frac{1}{n^h}\left[\frac{P_{H_2O}}{l}\left(p^h x_{H_2O} - p^l y_{H_2O}\right) - x_{H_2O} * J\right] \qquad \frac{dy_{H_2O}}{dA} = -\frac{1}{n^l}\left[\frac{P_{H_2O}}{l}\left(p^h x_{H_2O} - p^l y_{H_2O}\right) - y_{H_2O} * J\right]$$

$$J = \frac{P_{CO_2}(x_{CO_2})}{l}\left(p^h x_{CO_2} - p^l y_{CO_2}\right) + \frac{P_{N_2}(x_{N_2})}{l}\left(p^h x_{N_2} - p^l y_{N_2}\right) + \frac{P_{O_2}(x_{O_2})}{l}\left(p^h x_{O_2} - p^l y_{O_2}\right) + \frac{P_{Ar}(x_{Ar})}{l}\left(p^h x_{Ar} - p^l y_{Ar}\right) + \frac{P_{H_2O}(x_{H_2O})}{l}\left(p^h x_{H_2O} - p^l y_{H_2O}\right)$$

Figure 13. *Membrane model equations.*

where p^h and p^l represent feed and permeate pressure; $\frac{P_{CO_2}}{l}$, $\frac{P_{N_2}}{l}$, $\frac{P_{H_2O}}{l}$ permeances for CO_2, N_2 and H_2O, respectively; $n^h|_{A=0}$ feed flow rate; A_t membrane area; x_i, y_i each component's feed and permeate side concentrations, respectively.

This membrane model is then integrated with Excel and Aspen Plus, as shown in Figure 14. Initially, the feed and sweep stream conditions are defined within the Aspen Plus, along with the membrane block specifications. These conditions, along with membrane permeance values and iteration parameters, are then exported from Aspen Plus to Excel. After necessary unit conversions and reformatting of the data arrays, Excel provides input into the MATLAB. In MATLAB, a set of equations is solved to determine the membrane performance. Specifically, the membrane model

calculates the converged retentate and permeate flow rates and their gas compositions. The results from MATLAB are then returned to Excel. Finally, Excel conducts unit conversion and array formats back to Aspen Plus, allowing for process design and simulation.

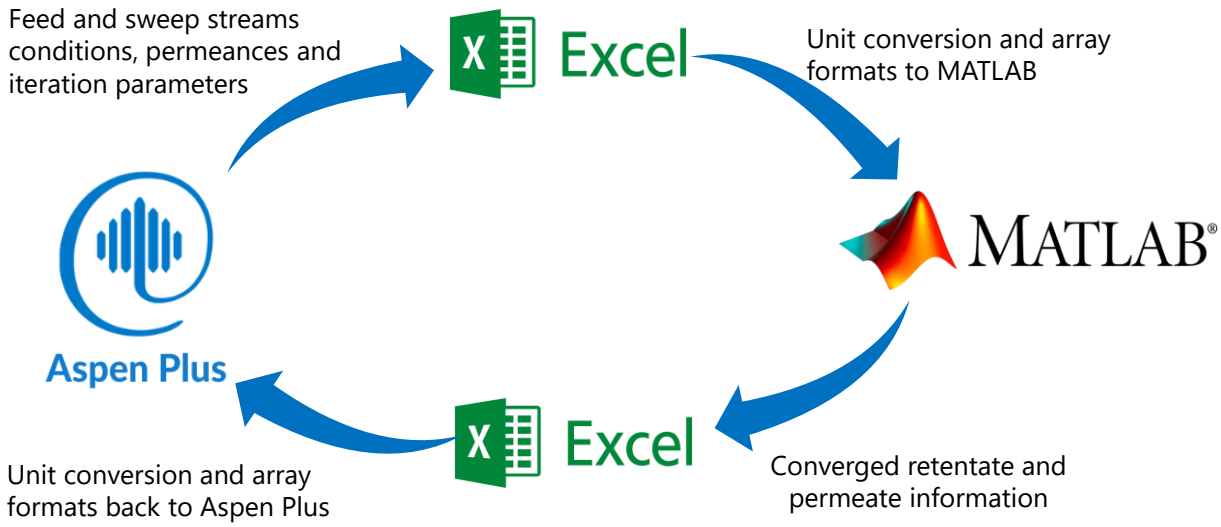

Figure 14. *MATLAB membrane model integrated with Aspen Plus and Excel for process simulation.*

Figure 15 shows an example of the MATLAB-Excel-Aspen Plus integration platform.

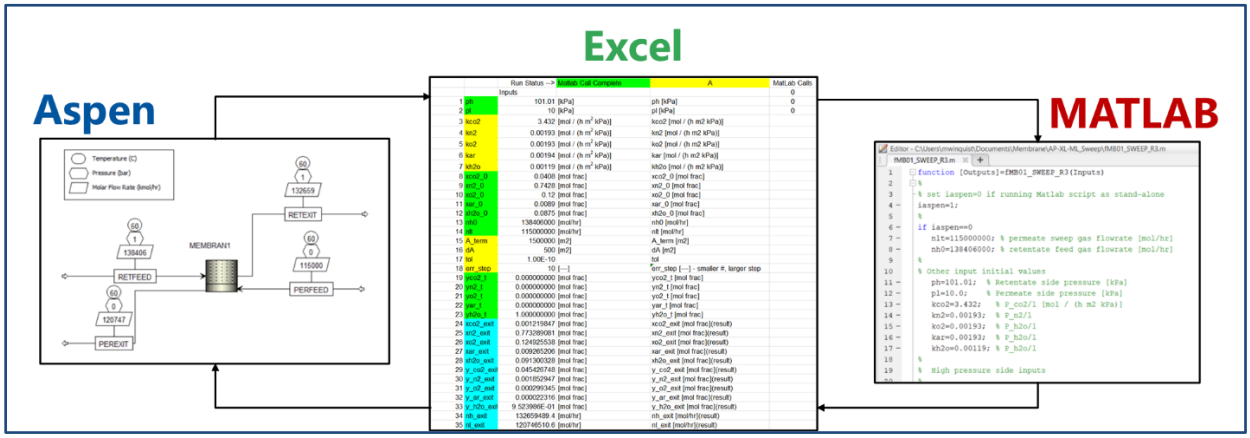

Figure 15. *A MATLAB-Excel-Aspen Plus integration platform.*

2.7. Techno-Economic Analysis

The design basis for a 97% CO_2 removal system utilizing the NCIL membrane-based process followed the guidance provided by the DOE National Energy Technology Laboratory's baseline report "NETL Rev 4a Baseline Report".[19] The reference cases, B31A and B31B.97, from the NETL Rev 4a baseline report represent a NGCC power plant without and with the implementation of CO_2 capture. Case B31A operates without CO_2 capture, whereas the Case B31B.97 achieves 97% CO_2 capture by using Shell CANSOLV® solvent technology.

Since Case B31B.97 is a solvent-based CO_2 capture process, the transformational NCIL membrane-based process is evaluated against it to support decision-making on the optimal CO_2 capture system.

In Case B31B.97, the power plant produces 636 MW_e net power after accounting for the parasitic power demand that the CANSOLV CO_2 capture process requires. The CANSOLV process is a commercially available, industry-standard CO_2 capture technology, and the plant size represents a commercial-scale greenfield application. The flue gas feed composition remains identical between Case B31B.97 and the NCIL membrane-based process.

Figure 16 illustrates the block flow diagram (BFD) for Case B31A, and Figure 17 represents the BFD for the NGCC power plant with the NCIL membrane-based CO_2 removal process, which has been developed to TRL 3 under the current project. The technical process inputs are detailed in Table 2.

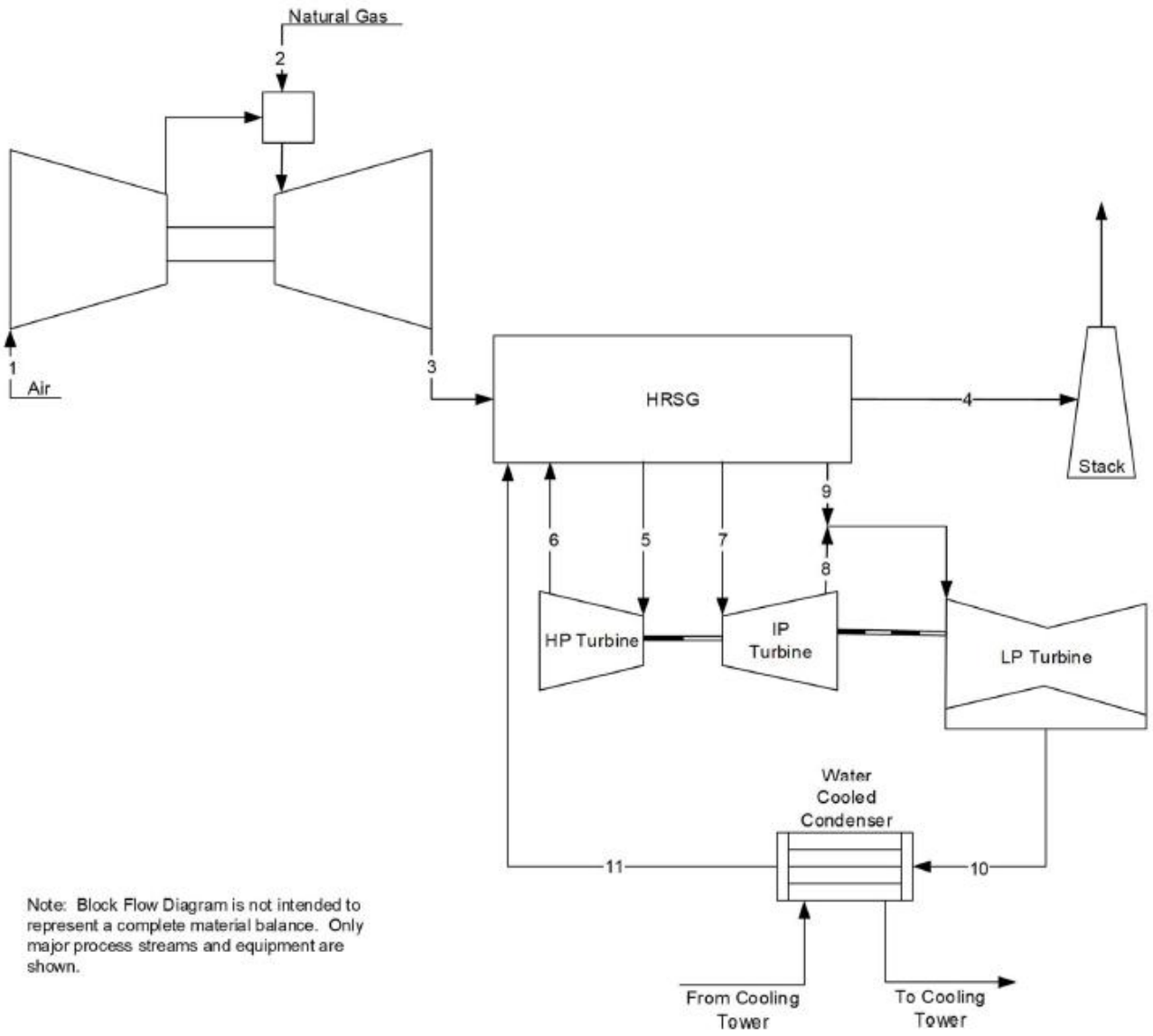

***Figure 16**. Base NGCC power BFD, Case B31A from the NETL report.*[19]

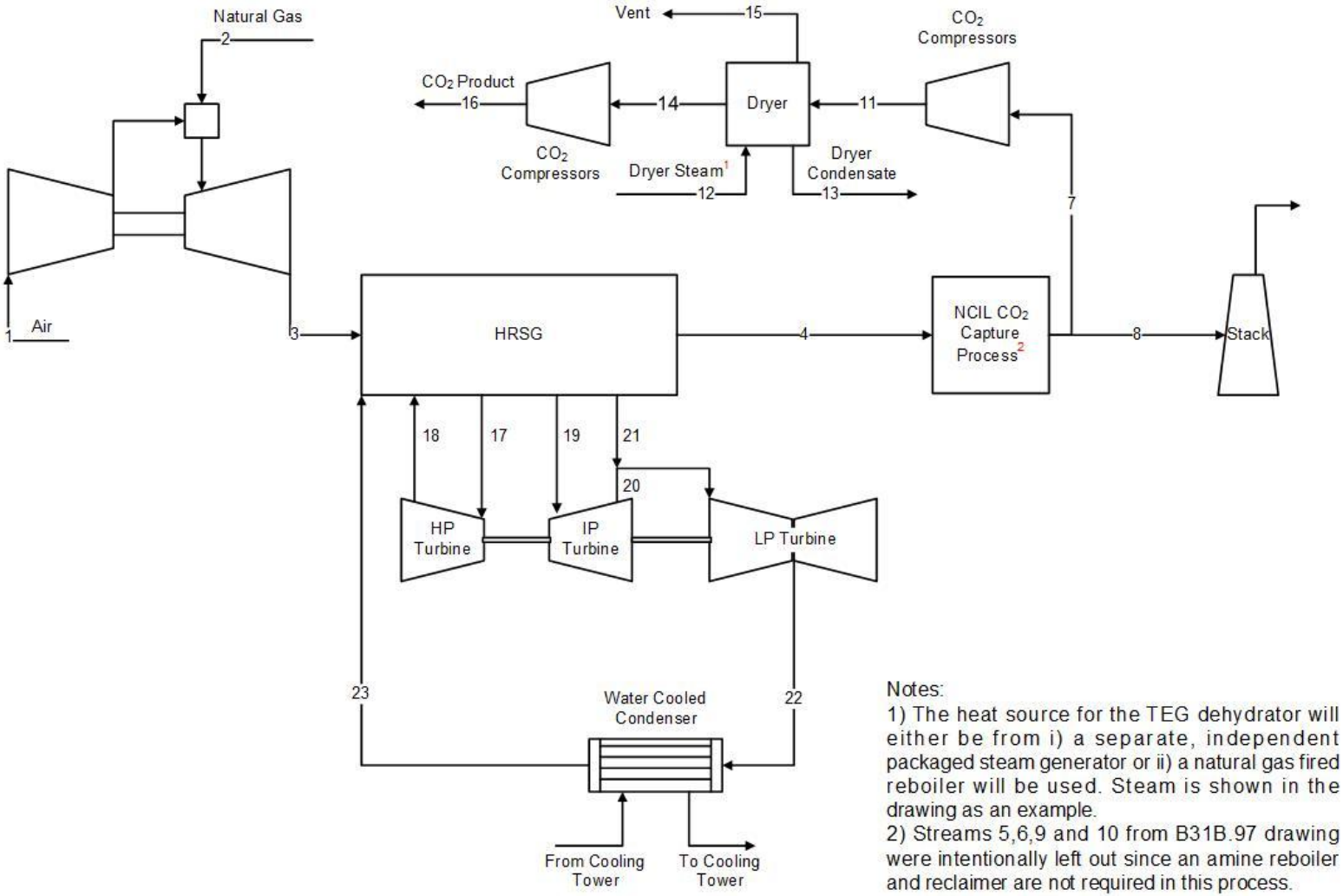

Figure 17*. NGCC power plant BFD with the transformational NCIL membrane process achieving 97% carbon capture.*

***Table 2**. Technical design basis.*

Description	SI		English		
	Unit	**Value**	**Unit**	**Value**	**Comment**
General					
Capacity Factor	%	85			DOE specification
CO_2 Removal	%	97			DOE specification
Stream Data					
Inlet Flue Gas					
Temperature	°C	100	°F	212	NETL Rev 4a Baseline Case B31B.97
Pressure	MPa	0.1	Psia	14.5	NETL Rev 4a Baseline Case B31B.97
Mass Flow Rate	kg/h	3,927,398	lb/h	8,658,430	NETL Rev 4a Baseline Case B31B.97
Composition					
CO_2	vol%	4.08			NETL Rev 4a Baseline Case B31B.97
H_2O	vol%	8.75			NETL Rev 4a Baseline Case B31B.97
N_2	vol%	74.28			NETL Rev 4a Baseline Case B31B.97
O_2	vol%	12			NETL Rev 4a Baseline Case B31B.97
Ar	vol%	0.89			NETL Rev 4a Baseline Case B31B.97
CO_2 in Inlet Gas	tonne/h	248	short ton/h	273	NETL Rev 4a Baseline Case B31B.97
Outlet CO_2 Specification					
Temperature	°C	30	°F	86	DOE specification
Pressure	MPa	15.27	Psia	2,215	DOE specification
CO_2	mol%	>95%			DOE specification
Cooling Water					
Supply Temperature	°C	15.6	°F	60	NETL Rev 4a Baseline Case B31B.97
Return Temperature	°C	26.7	°F	80	NETL Rev 4a Baseline Case B31B.97
Capture System Stream – No Major Stream users					
Membrane Performance and Specs					
NCIL Membrane					
Temperature	°C	70	°F	158	UB specification
CO_2 Permeance			GPU	2,700	UB specification
CO_2/N_2 Selectivity				2,200	UB specification
H_2O Selective Membrane					
Temperature	°C	110	°F	230	UB specification
H_2O Permeance				11,000	UB specification
H_2O/CO_2 Selectivity				1,000	UB specification

3. Results and Discussion

3.1. NCIL Membrane Fabrication and Characterization

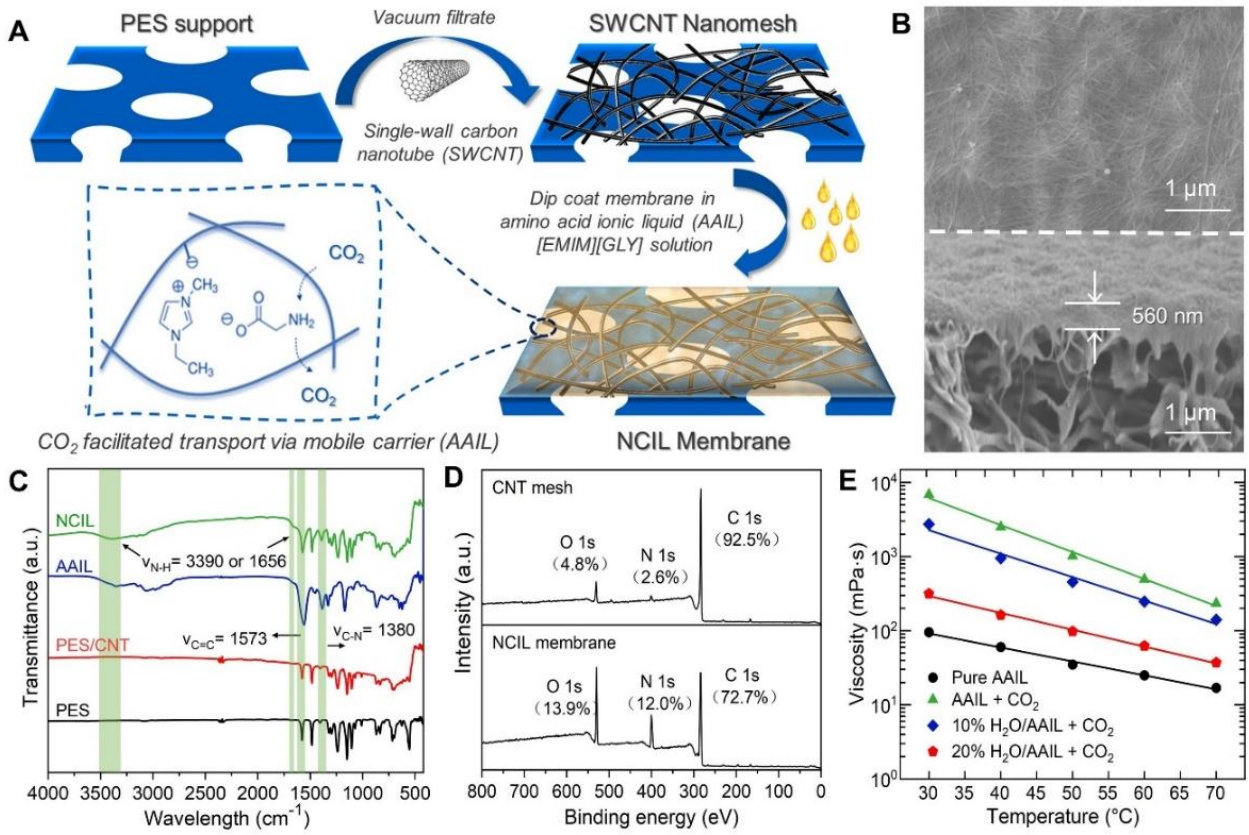

***Figure 18**. Conceptual design and characterization of NCIL membrane. (A) Schematics of the NCIL flat sheet membrane fabrication procedure and facilitated CO_2 transport via mobile carrier AAIL; (B) Surface and cross-sectional SEM images of a representative NCIL membrane; (C) FTIR spectra of pristine PES support, CNT/PES membrane, AAIL ([Emim][Gly]), and NCIL membrane; (D) XPS full spectra of the CNT/PES membrane (top), and NCIL membrane (bottom); and (E) Viscosity of pure [Emim][Gly] and [Emim][Gly]/H_2O mixture before and after purging with CO_2. NCIL membranes used for characterization were prepared with a CNT loading density of 60 mg m^{-2} and an IL solution of 150 mg mL^{-1} for dip-coating.*

Figure 18A illustrates the facile preparation of a flat-sheet NCIL membrane via dip-coating of a CNT mesh into an IL solution. With solvent evaporation, the capillary force provided by the CNT mesh is expected to draw the amine-functional IL into its nanopores for stable facilitated CO_2 transport.[20]

Figure 18B shows a defect-free surface morphology and a membrane thickness of 560 nm of a representative NCIL membrane. EDS characterization further demonstrated the preferential concentration of IL, according to the N atoms derived from the IL, into the top CNT mesh to form a continuous layer rather than within the support (Figure 19).

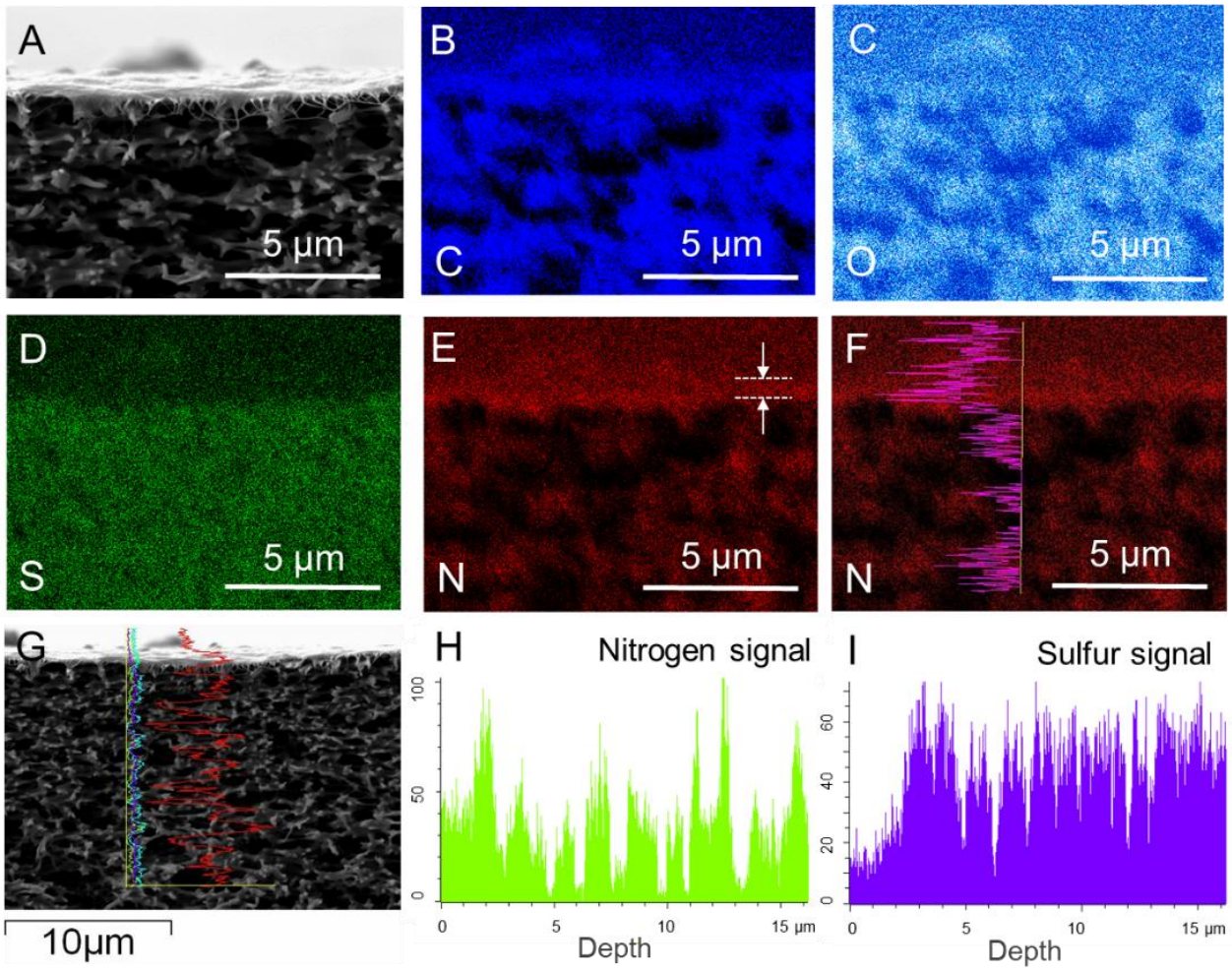

Figure 19*. SEM and EDS images of nanoconfined NCIL membrane. (A) cross-section image of membrane; (B)-(F) EDS elemental mapping for C, O, S and N elements; (E) EDS elemental mapping and line scanning patten for N element; and (G)-(I) EDS line scanning patterns and N, S elements density distribution in different part of the membrane. EDS results indicate that ionic liquid [Emim][Gly] is concentrated on the top of support to form continuous thin membrane layer.*

The surface chemistry was further analyzed by Fourier-transform Infrared (FTIR) spectroscopy, as shown in Figure 18C. Compared with the plain PES support and the CNT mesh, new peaks appeared at 3,390 cm^{-1}, 1,656 cm^{-1}, and 1,380 cm^{-1} for the NCIL membrane. This can be attributed to the primary amine and C-N bond from [Emim][Gly], which also possesses strong FTIR absorption peaks at these three wavelengths.[21]

Similarly, Figure 18D shows that compared to the CNT mesh, XPS spectrum of the NCIL membrane had more intensified nitrogen element peak due to the introduction of amine functional groups.

To better understand immobilization and fluidity of IL in the NCIL membrane, the viscosity of [Emim][Gly] and [Emim][Gly]/H_2O mixture was measured. As shown in Figure 18E, lower temperature induced viscosification of the AAIL, whereas the addition of a small amount of water significantly reduced its viscosity. Interestingly, viscosity of the AAIL increased dramatically by

almost two orders of magnitude when CO_2 was introduced, probably due to the strong intermolecular interaction between CO_2 and the amine functional groups.[22] Clearly, the viscosity and corresponding mobility of the AAIL in NCIL membrane are expected to depend strongly on the operation conditions, such as temperature, water content, and CO_2 concentration, and their influence on the nanoconfined AAIL resistance to the pressure-driven flow in the CNT mesh will be further discussed in the gas separation section.

3.2. Highly Permeable CNT Mesh Construction for Effective Nanoconfinement

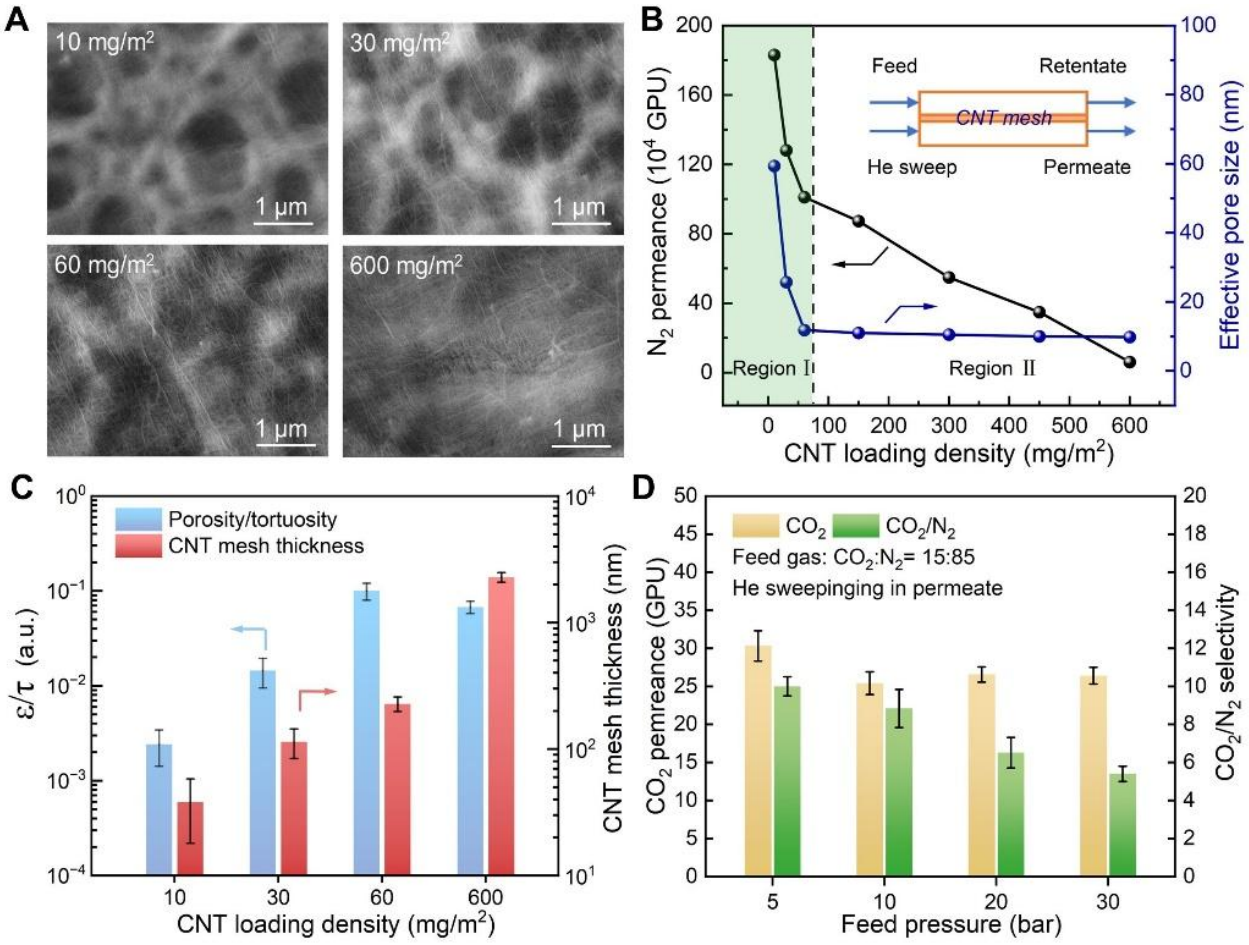

Figure 20. *Effect of CNT loading density on physical and gas permeation properties of nanoconfined structure. (A) Surface SEM images of the CNT mesh deposited on the PES support with CNT loading density ranging from 10 to 600 mg* m^{-2}*; (B)* N_2 *permeation under 1.5 bara feed pressure at 70°C and effective pore size of the CNT mesh (Insert: Gas permeation measurement unit for* N_2*. Region I: Pore size control region; Region II: Thickness control region); (C) CNT mesh thickness and structure-relevant* ε/τ *factor as a function of CNT loading density; and (D) Gas separation performance of the NCIL membrane under high pressure, prepared with a CNT loading density of 60 mg* m^{-2} *and an IL solution of 150 mg* mL^{-1} *for dip-coating.*

CNT nanomesh deposition and its nanostructures at different CNT loadings were first investigated prior to IL loading. Figure 20A shows the morphology of the CNT mesh corresponding to different CNT loading densities (CNT mass per membrane area). A defective mesh was obtained when the CNT loading density was below 10 mg m^{-2} (Figure 21), while further increasing the loading density by 3, 6, and 60 times resulted in denser and more compact nanostructures, making the substrate less visible. We also found that the thickness of the CNT mesh increased linearly with the CNT loading density (Figure 22), indicating the unchanged porosity of the CNT mesh.

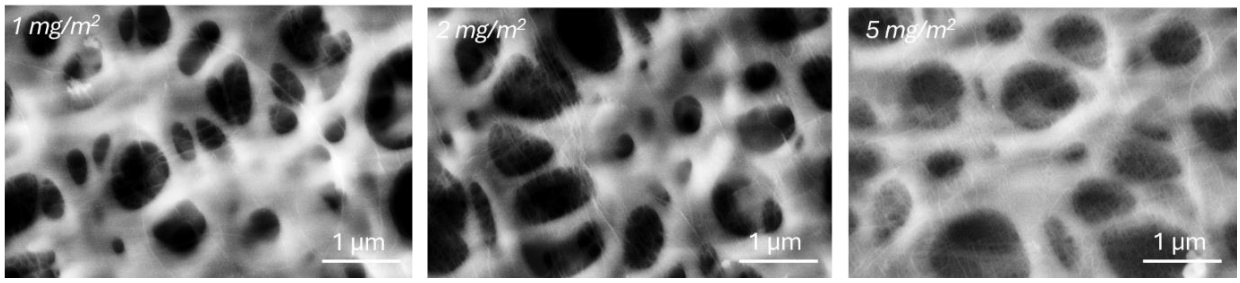

Figure 21. *Surface SEM images of the CNT mesh coated onto PES support. CNT loading density ranges from 1 mg m^{-2} to 5 mg m^{-2}, exhibiting the gradual formation of dense CNT film.*

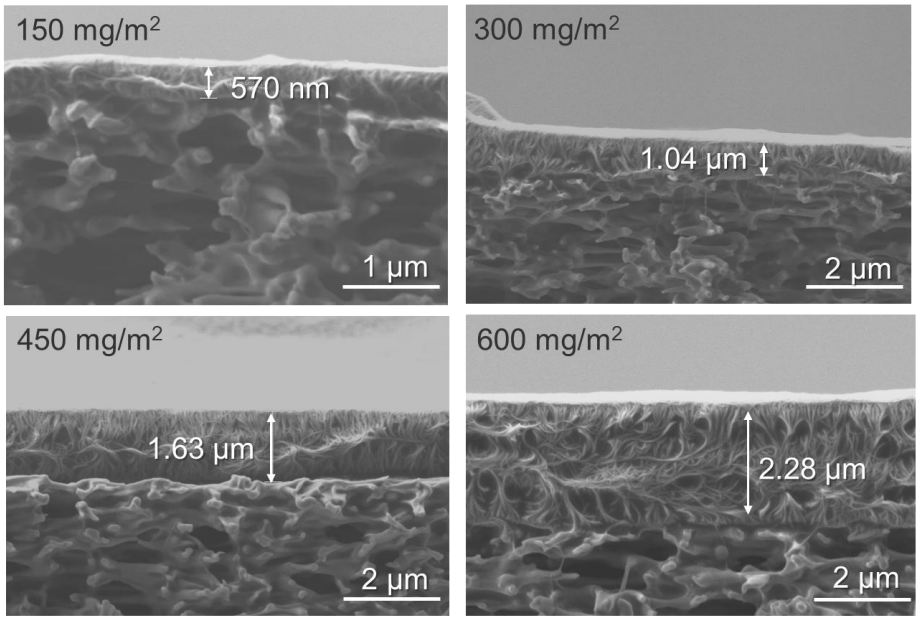

Figure 22. *Cross-sectional SEM images of the CNT mesh coated onto PES support. CNT loading density ranges from 150 mg m^{-2} to 600 mg m^{-2}. The thickness of CNT mesh increased linearly with CNT loading density when CNT mesh thickness is greater than 500 nm.*

The microstructure of the resulting CNT mesh was further examined through MWCO characterization, which is based on the rejection of Polyethylene Glycol (PEG) with varying molecular weights at 0.5 bara feed side pressure. As shown in Figure 20B, the effective pore size of the CNT mesh dramatically decreased from 59 to 11 nm with the increase of the CNT loading density from 10 to 60 mg m^{-2}, and then only decreased slightly to 9.8 nm even after increasing CNT loading density by 10 times. The N_2 permeation test was conducted to reveal ultralow gas

transport resistance of the CNT network with N_2 permeance up to 10^6 GPU (GPU: gas permeation unit; 1 GPU= 3.35×10^{-10} mol $(m^2\cdot s\cdot Pa)^{-1}$), and its corresponding change with different CNT loading density (Figure 20B). Two distinct regions of N_2 permeance decline with increasing CNT loading density were identified, suggesting a transition in the nanostructure of the CNT mesh and a corresponding shift in transport resistance behavior. Based on the variations in pore size and thickness with increasing CNT loading density, the two distinct regions of N_2 permeance decline can be attributed to a pore size-controlled region and a thickness-controlled region, respectively. Therefore, the optimal CNT mesh is expected at a CNT loading density of 60 mg m^{-2}, the transition point of two regions, offering low transport resistance while effectively confining the IL for enhanced mechanical stability.

To further elucidate the inherent transport resistance of our nanoconfined networks, we introduced the structure-relevant ε/τ factor. As discussed in our previous work,[23], the ε/τ factor was calculated based on the pore-flow model, also known as Hagen-Poiseuille equation:[24]

$$Permeance = \frac{J}{\Delta P} = \frac{\pi \varepsilon r_p^2}{8\mu\delta\tau} \quad (12)$$

Where J is flux, ΔP transmembrane pressure drop, ε surface porosity, r_p pore radius, μ solvent viscosity, δ membrane thickness, and τ transport channel tortuosity. In this case, high ε/τ factor implied high density of nanopores with low tortuosity and boosted transport property.[23] Given the calculated pore radius from MWCO and the measured mesh thickness by SEM, the ε/τ factor of CNT mesh was calculated using water permeation data at 0.5 bar pressure drop (Figure 23).

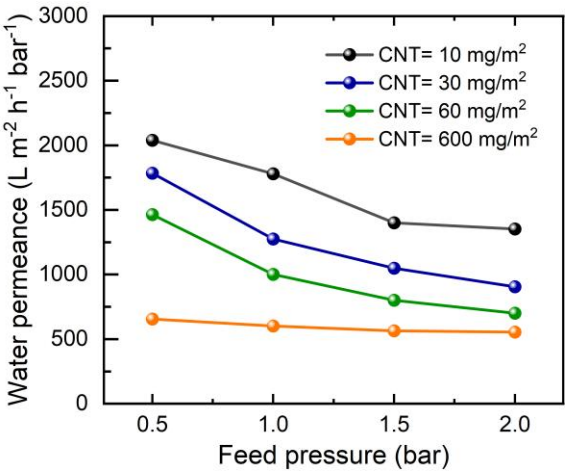

***Figure 23**. Water permeance of CNT mesh coated PES membrane under different feed pressures. The figure showed compressibility of CNT mesh under pressure. Thicker CNT membrane can handle higher pressure without obvious structure deformation.*

Figure 20C shows a maximum ε/τ factor close to 0.1 at a CNT loading density of 60 mg m^{-2}, outperforming other nanoconfined network (see details in Table S1, Appendices).

Meanwhile, the nanoconfinement effectiveness of the CNT network was demonstrated via calculated theoretical breakthrough pressure, following the simplified Young-Laplace equation:[25]

$$Breakthrough\ Pressure = BP = \frac{2\gamma cos\theta}{r_p} \quad (13)$$

Where γ is surface tension of liquid,[26], and θ the contact angle between the liquid and the pore surface (Figure 24). The calculated breakthrough pressures demonstrated the high-pressure

tolerance of the CNT mesh-confined IL membrane >25 bar, which was further validated through continuous pressurization and depressurization tests after loading IL into the optimized CNT mesh with a 60 mg m^{-2} CNT loading density.

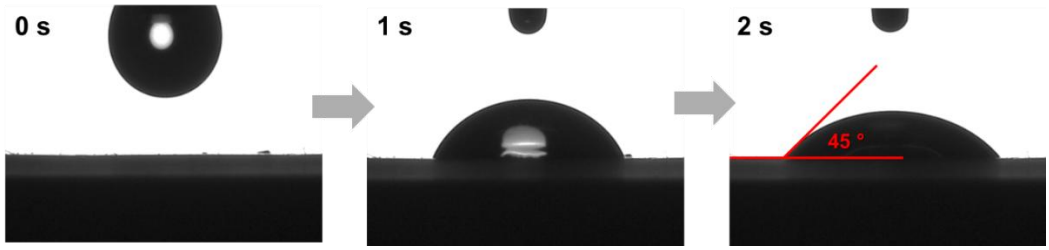

Figure 24. *Contact angle of ionic liquid [Emim][Gly] onto CNT mesh coated PES membrane. The CNT loading density onto PES was controlled at 60 mg* m^{-2}.

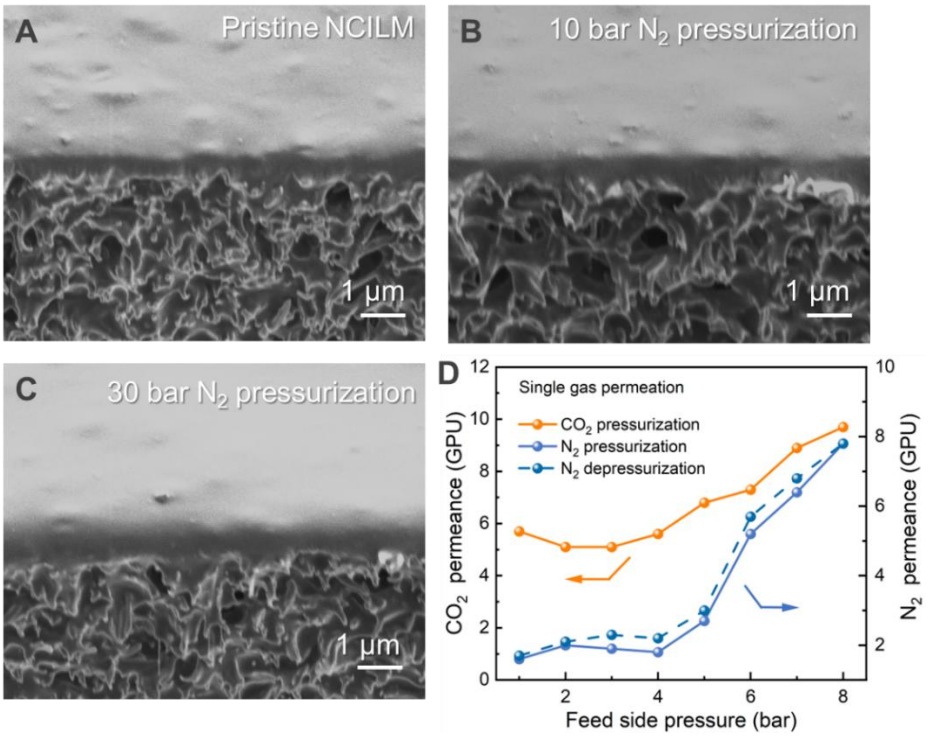

Figure 25. *Demonstration of effective nanoconfinement of ionic liquid within the NCIL membranes. (A)-(C) Cross-sectional SEM images of the NCIL membrane before and after high pressurization test; (D) Reversible gas permeation test after pressurization and depressurizations process.*

Figure 25A-C shows that the membrane thickness remained unchanged at 420 nm after pressurization under 10 bara of N_2. An increase of N_2 pressure up to 30 bara failed to displace the IL from the nano-space of the CNT mesh, indicating strong nanoconfinement. Figure 25D shows reversible N_2 permeation during a pressurization and depressurization cycle.

Figure 20D further demonstrates almost constant CO_2 permeance even under 30 bara of pressurization with an increase in N_2 permeance from 3 to 4.8 GPU, further implying the excellent mechanical stability of the confined ionic liquid-based membrane.

3.3. Ionic Liquid Regulation for Defect-free NCIL Membrane Fabrication

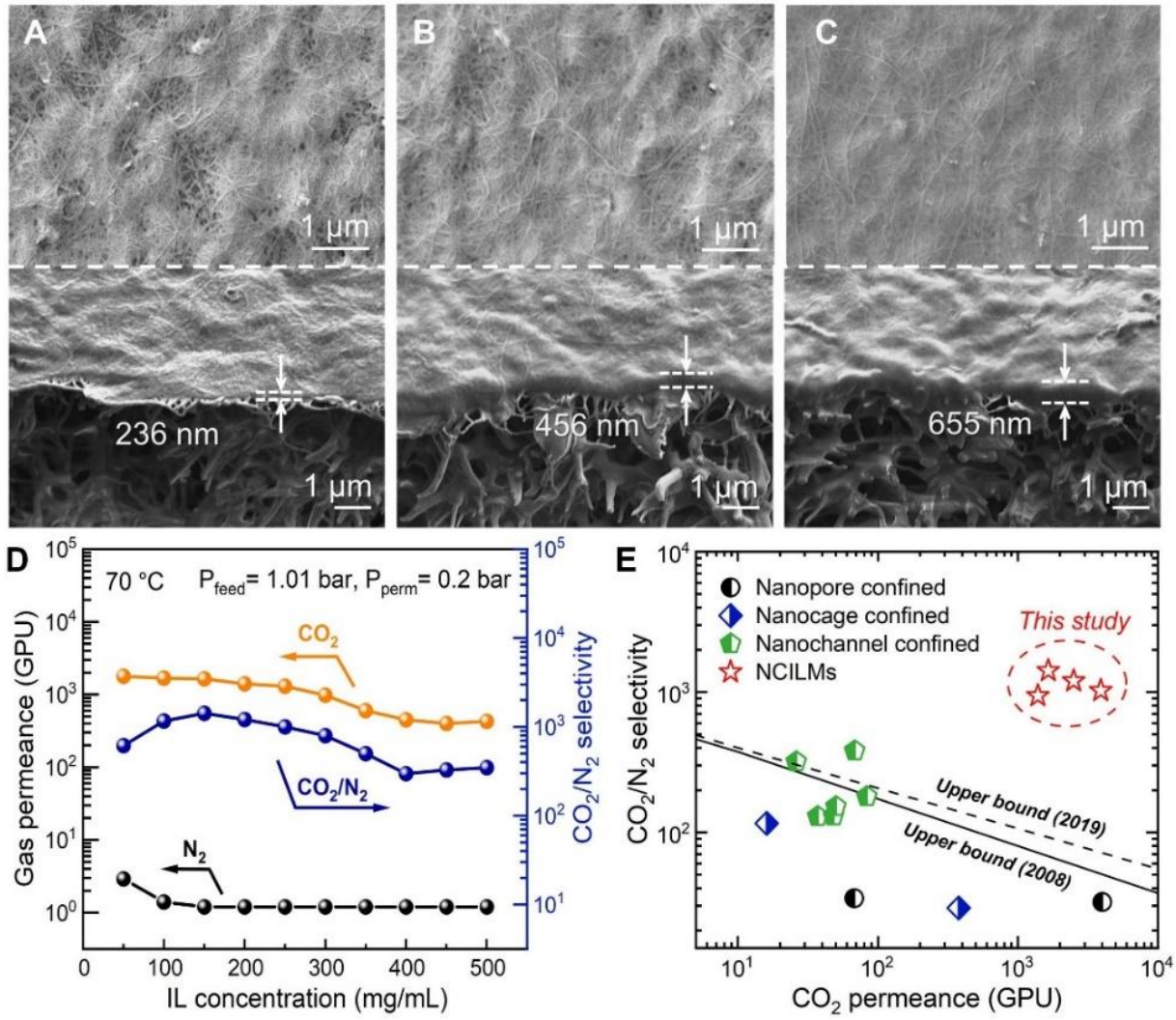

***Figure 26**. Effect of IL loading on morphology and gas separation performance of the NCIL membrane. (A-C) Surface and cross-sectional SEM images of the NCIL membranes fabricated using varying IL concentrations of 50 (A), 100 (B) and 150 (C) mg mL^{-1}, respectively; (D) Gas separation performance of the NCIL membranes as a function of IL concentration in the coating solution; (E) Gas separation performance comparison with reported nanoconfined IL-based membranes for CO_2/N_2 separation (Data points are summarized in Table S2, Appendices). The 2008 and 2019 upper bounds were shown as the black solid and dash lines, respectively; membrane thickness was assumed to be 100 nm for converting permeability into permeance. Unless otherwise specified, NCIL membranes were prepared with a CNT loading density of 60 mg m^{-2} and an IL solution of 150 mg mL^{-1} for dip-coating. NCIL membranes were tested using simulated flue gas (4.2% CO_2, saturated H_2O vapor, and balanced N_2) under 1.01 bara feed pressure and 0.2 bara permeate side pressure at 70°C.*

Building on the optimized, high-efficiency gas transport CNT mesh, AAIL was sequentially loaded in nanoconfined space to form a defect-free, thin film membrane. Figures 26A-C shows the gradual filling of IL onto the CNT mesh as IL concentration in the coating solution increases from 50 to 150 mg mL^{-1}. The accumulated IL loading also swelled the CNT mesh, leading to an

expanded NCIL membrane with thickness from 236 to 656 nm. However, further introducing the IL loading by adding more IL in the coating solution did not linearly expand the CNT/IL selective layer. Instead, it led to IL penetration into the support, blocking the transport pathways (Figures 27 and 28).

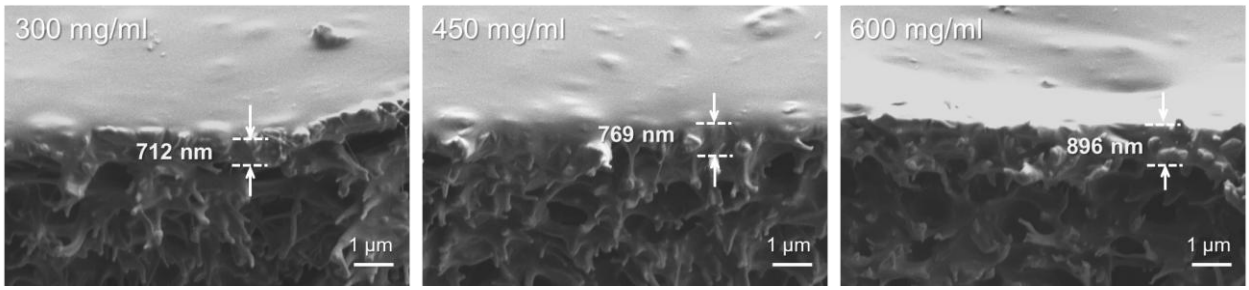

***Figure 27**. Cross-sectional SEM images of the NCIL membranes. The membranes were prepared with different concentrations of IL coating solutions ranging from 50 to 600 mg mL^{-1} with CNT loading density of 60 mg m^{-2}.*

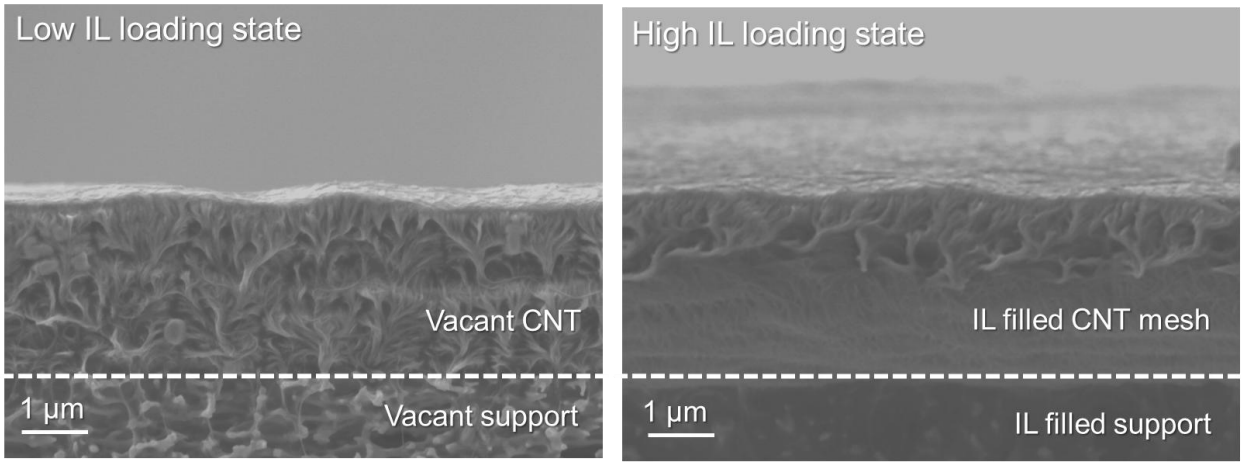

***Figure 28**. Cross-sectional SEM images of NCIL membranes. The membranes were prepared with different concentrations of IL coating solutions ranging from 150 to 450 mg mL^{-1} with CNT loading density of 600 mg m^{-2}.*

To further understand the influence of IL loading, the gas separation performance of the NCIL membranes for simulated natural gas flue gas was evaluated. Specifically, the NCIL membranes were tested at 70°C using simulated flue gas composed of 4.2% CO_2, saturated H_2O vapor, and N_2 as a balance gas, under a feed pressure of 1.01 bara and a permeate pressure of 0.2 bara. As shown in Figure 26D, CO_2 permeance decreased gradually with the increase of IL loading, probably due to the increased CO_2 transport resistance as suggested by Figures 26A to 26C. On the other hand, N_2 permeance initially decreased, apparently because of the pore filling of IL, and then remained nearly constant. Since the high loading of IL eventually saturated the polymeric support without further swelling the CNT mesh, the gas permeance of the NCIL membrane plateaued at high IL concentrations in coating solution. Thus, the optimal IL concentration was identified as 150 mg mL^{-1} for forming a continuous and uniform selective layer with the highest CO_2 permeance.

Figure 26E compares the optimized NCIL membranes with the reported nanoconfined IL-based membranes for CO_2/N_2 separation. Due to the highly efficient nanoconfinement of ILs, most IL-based membranes with ~1 nm pores/nanochannels exhibit high CO_2/N_2 selectivity but limited CO_2 permeance. In contrary, the NCIL membranes in this work demonstrated rapid CO_2 transport property while maintaining high CO_2/N_2 selectivity, indicating the high gas separation efficiency of this nanoconfined IL-based design.

3.4. Superior Gas Separation Performance of the NCIL Membrane

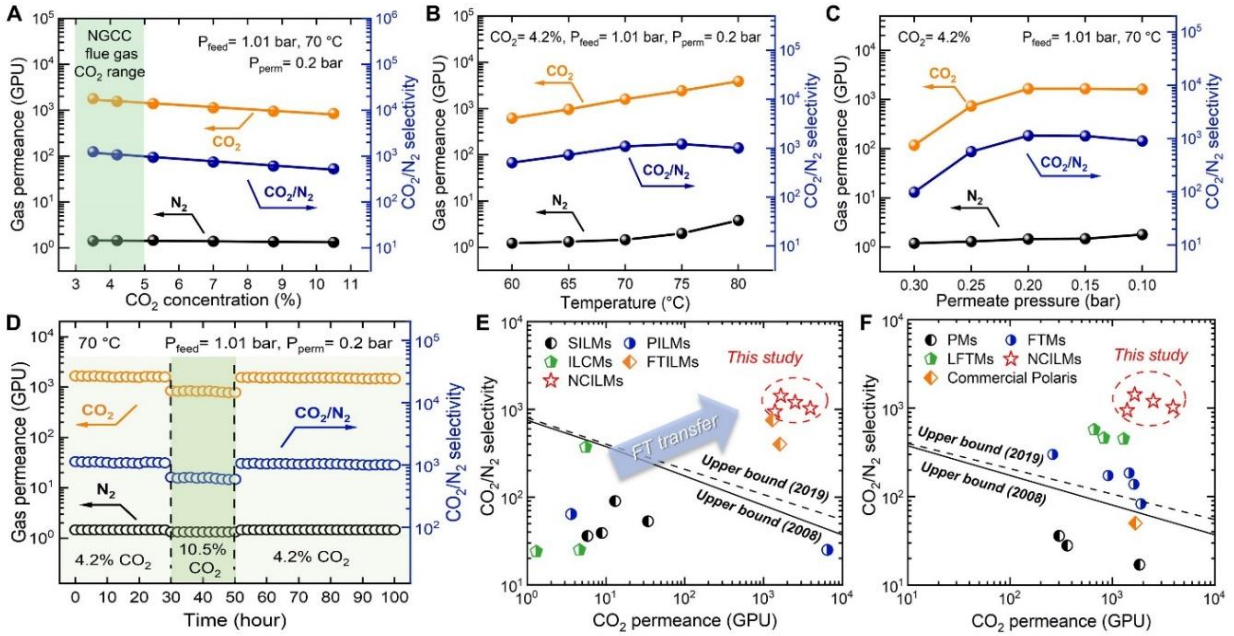

Figure 29. *Suprior and stable CO_2/N_2 mixed gas separation performance of the NCIL membrane. (A) Influence of CO_2 concentration in the feed gas; (B) Influence of operation temperature; (C) Influence of permeate side pressure; (D) Long-term stability of the NCIL membrane; green highlighted zone indicates the change of CO_2 concentration in the feed gas; (E) Gas separation performance comparison with the reported IL-based membranes for CO_2/N_2 separation (Data points are summarized in Table S3, Appendices); and (F) Gas separation performance comparison with the reported thin film polymeric and facilitated transport membranes for CO_2/N_2 separation (Data points are summarized in Table S4, Appendices). The 2008 and 2019 upper bound limits were shown as black solid and dash lines,[27,28] respectively; membrane thickness was assumed to be 100 nm for converting permeability into permeance. The NCIL membrane was prepared with 60 mg m^{-2} CNT loading density and 150 mg mL^{-1} IL solution for dip-coating. Unless otherwise specified, NCIL membrane was tested using simulated flue gas composed of 4.2% CO_2, saturated H_2O vapor, and balanced N_2 under 1.01 bara feed pressure and 0.2 bara permeate side pressure at 70°C.*

The influence of operation conditions on separation properties of the NCIL membranes were investigated. As shown in Figure 29A, CO_2 permeance declined almost exponentially from 1,780 to 850 GPU when the CO_2 feed concentration increased from 3.5% to 10.5%. The characteristic CO_2 saturation behavior of gas transport agents under elevated CO_2 partial pressure reflects the facilitated transport mechanism enabling CO_2 permeation through the NCIL membrane. In contrast, N_2 permeance only decreased slightly with the decrease of N_2 partial pressure resulting

from the increased CO_2 concentration. This can be attributed to the solution-diffusion mechanism that inert gases usually follow. Thus, the CO_2/N_2 selectivity also decreased exponentially with increasing CO_2 concentration, following the same trend as the change in CO_2 permeance.

The characteristic permeance trends of the facilitated transport gas (CO_2) and inert gas (N_2) under elevated feed pressure are shown in Figure 30. CO_2 permeance decreased from 1,550 to 520 GPU, while N_2 permeance increased from 1.5 to 15 GPU as the feed pressure increased from 1.01 bara to 2 bara, with a constant CO_2 and N_2 concentrations in the feed. In summary, the NCIL membranes exhibited superior separation performance, with CO_2 permeance of 1,550 GPU and CO_2/N_2 selectivity of 1,070 within 3-5% CO_2 concentration and at 1.01 bara feed pressure, highlighting their potential as ideal candidates for CO_2 capture from natural gas flue gas.

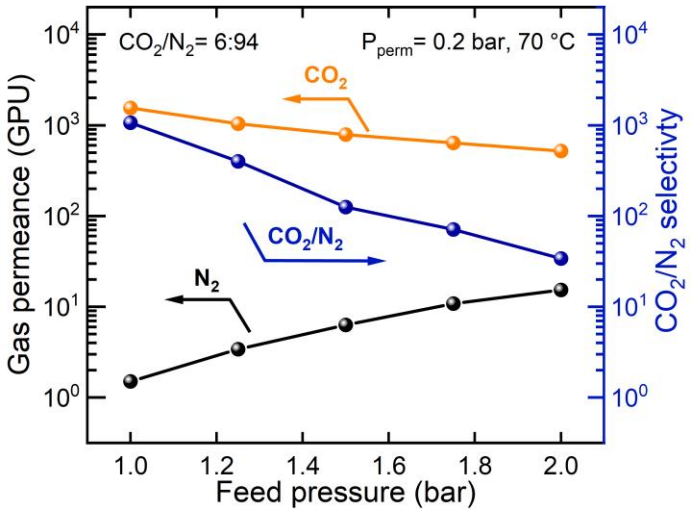

***Figure 30**. Gas separation performance of NCIL-C60/IL150 membrane as a function of feed pressure in feed side. PAIL membranes were tested using simulated flue gas composed of 4.2% CO_2, saturated H_2O vapor, and balanced N_2 under 0.2 bara permeate side pressure, 70°C.*

The dependence of temperature and permeate side pressure on CO_2 separation performance of the NCIL membrane was then examined. As shown in Figure 29B, increasing the temperature from 60 to 80°C, a typical temperature range for CO_2 capture from natural gas flue gas, leading to an exponential increase in CO_2 permeance from 620 GPU to 3,860 GPU; the calculated activation energy under fully saturated conditions was 86.2 kJ mol^{-1} (Figure 31). On the other hand, N_2 permeance increased from 1.20 to 3.80 GPU after 75°C, resulting in a slight drop of CO_2/N_2 selectivity. This change can be attributed to the improved mobility of the IL-specifically, the decreased viscosity under elevated temperature, which facilitated faster CO_2 transport and slightly "loosened" the NCIL membrane structure.

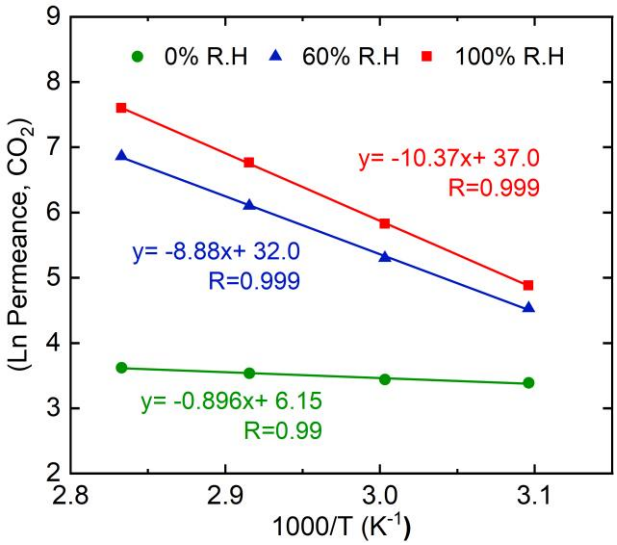

***Figure 31**. The ln (Permeance, CO_2) – 1/T plot for CO_2 permeation activation energy of the NCIL membrane under different relative humidity (R.H). The feed gas composed of 10.5 vol% CO_2, 0~31.2 vol% H_2O and balanced N_2 was continuously measured at 0.2 bara permeate side pressure, 70°C. Feed side pressure was controlled at 1.01 bara.*

Figure 29C shows the membrane separation performance at different permeate side pressures. Lower permeate side pressure increased the trans-membrane driving force for gases and promoted CO_2 transport. Therefore, the CO_2 permeance increased from 120 to 1,700 GPU. Unlike CO_2 possessing high binding energy with amine-based carriers, N_2 exhibited negligible intermolecular interaction with AAIL.[29] As a result, only negligible change in N_2 permeance was observed with decreasing permeate pressure, while the CO_2/N_2 selectivity followed a trend similar to that of the CO_2 permeance, reaching a maximum selectivity of 1,100 at a permeate-side pressure of 0.2 bara.

The long-term stability of the NCIL membrane for CO_2/N_2 gas mixture separation was evaluated under simulated flue gas conditions. As indicated in Figure 29D, the NCIL membrane was stable for the first 30 h and showed a CO_2 permeance of 1,700 GPU and a CO_2/N_2 selectivity of 1,100 for CO_2 capture from simulated natural gas flue gas containing 4.2% CO_2. Then, the CO_2 concentration was increased to 10.5% to mimic CO_2 capture from coal-fired flue gas, and the NCIL membrane exhibited a stable CO_2 permeance of 820 GPU and CO_2/N_2 selectivity of 620 during 20-h continuous testing. The separation performance of the NCIL membrane recovered its initial performance after switching CO_2 concentration to 4.2% and remained stable for 50 h.

Figure 29E compares the NCIL membranes with traditional IL-based membranes reported in the literature for CO_2/N_2 separation. Owing to the combination of rapid gas transport channels and facilitated transport characteristics, the NCIL membranes surpass the Robsen upper bound and outperform traditional IL-based membranes. Furthermore, the NCIL membranes demonstrated significantly superior CO_2/N_2 separation performance compared to most state-of-the-art polymeric and facilitated transport-based membranes (Figure 29F and Table S4 in the Appendices), indicating this class of membranes may serve as the next generation of rapid CO_2 transport membranes for capturing CO_2 from lean-concentration point sources.

3.5. Natural Gas Flue Gas Separation using 75-cm^2 NCIL membranes

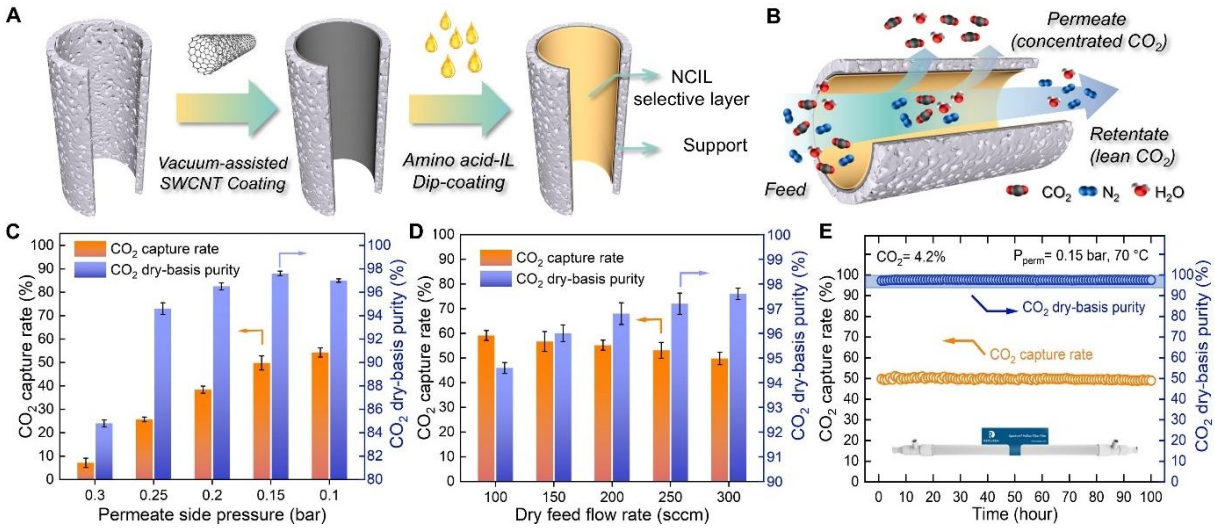

Figure 32. *Scaleup of the NCIL membrane. (A) Schematics of the hollow fiber NCIL membrane fabrication procedure; (B) illustration of CO_2 transport through the resulting membrane. The CO_2/N_2 mixed gas separation performance of the NCIL hollow fiber membrane as a function of membrane operation conditions: (C) Influence of permeate side pressure; (D) Influence of dry feed flow rate; and (E) Long-term stability of the NCIL membrane (Insert: Photo of a 75 cm^2 hollow fiber module). The NCIL membrane was prepared with 60 mg m^{-2} CNT loading density and 150 mg mL^{-1} IL solution for dip-coating. Unless otherwise specified, the memrane was tested using simulated flue gas composed of 4.2% CO_2 (6% dry-basis), saturated H_2O vapor, and balanced N_2 under 1.01 bara feed pressure and 0.15 bara permeate side pressure at 70°C, with feed gas flow rate of 200 standard cubic centimeter per minute (sccm).*

To explore the potential for large-scale application, we further developed the NCIL membrane by coating it onto the inner surface of a 75 cm² hollow fiber Polyether Sulfone (PES) support, leveraging the high packing density and scalability of hollow fiber modules.[30] Similar membrane fabrication procedure as that of the flat sheet membrane was followed, including vacuum-assistant CNT coating and IL solution dip-coating (Figure 32A).

Figure 33 shows SEM images of the substrate, CNT coated substrate and the resulting membrane. The separation properties of the NCIL hollow fiber membrane were tested at 70°C using 1.01 bara simulated natural gas flue gas (4.2% CO_2, saturated H_2O vapor, and balanced N_2) as feed gas under 0.15 bara permeate side pressure outside of hollow fiber membrane (Figure 32B).

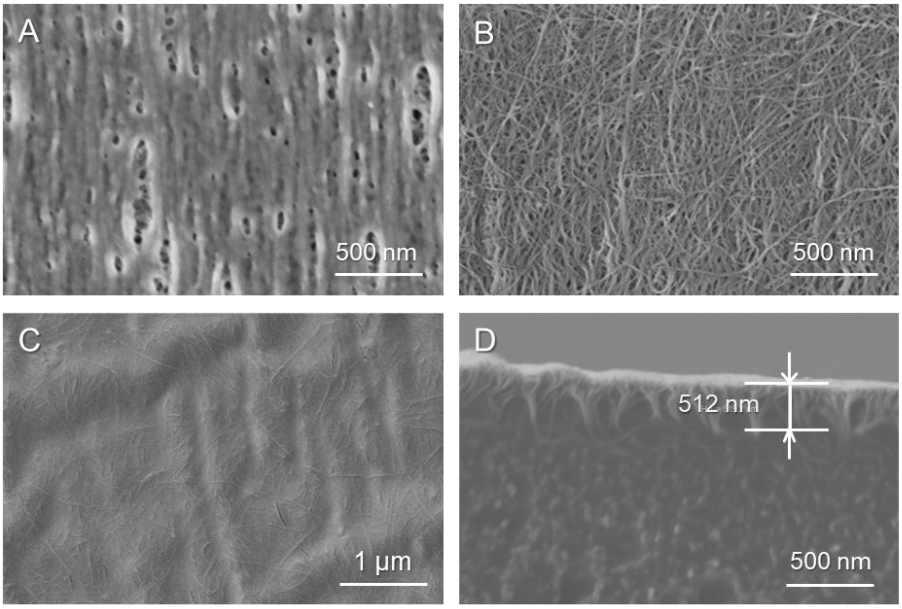

***Figure 33**. SEM images of scaled-up hollow fiber NCIL membranes. (A) 75 cm^2 hollow fiber PES support (300 kDa); (B) CNT loaded hollow fiber support (60 mg m^{-2} CNT loading density); (C) Surface SEM image of the NCIL hollow fiber membrane (450 mg mL^{-1} IL concentration in coating solution); and (D) Cross-sectional SEM image of NCIL membrane.*

Apart from ultra-high CO_2 permeance and CO_2/N_2 selectivity, CO_2 capture rate and CO_2 dry-basis purity in permeate side were also evaluated for potential industrial application purposes. As shown in Figure 32C, the NCIL membrane demonstrated its capability to enrich CO_2 from 4.2% to 98% in a single step, owing to its ultra-high CO_2/N_2 selectivity. Decreasing the permeate side pressure from 0.3 bara to 0.15 bara enabled larger driving force for rapid CO_2 transport, thus improving CO_2 capture rate from 7.1% to 49.8% and CO_2 dry-basis purity from 84.1% to 97.6%. The CO_2/N_2 selectivity was 2,000, and the CO_2 permeance was 2,300 GPU for a permeate side pressrue of 0.15 bara.

Meanwhile, the separation performance of the NCIL membrane could be further enhanced by mitigating concentration polarization-defined as the accumulation of slower-permeating species (N_2) near the membrane surface due to the depletion of the preferentially permeating species (CO_2), which is particularly pronounced in fast CO_2 transport, highly selective membranes operating at a stage cut. The resulting decrease in CO_2 and increase in N_2 driving forces typically lead to reduced CO_2/N_2 selectivity and diminished CO_2 flux. In this case, increasing feed flow rate facilitates CO_2 bulk diffusion towards the membrane surface and thus increases the CO_2 flux. As shown in Figure 32D, increasing the feed gas flow rate from 150 to 300 sccm improved CO_2 dry-basis purity from 94.6% to 97.6%, while the CO_2 capture rate decreased from 59.1% to 49.8%, indicating the enhanced CO_2 separation capability at the expense of capture efficiency.

The long-term stability test of the 75 cm^2 hollow fiber membrane was performed, as shown in Figure 32E. The results revealed only a slight decrease in CO_2 capture rate (from 50.3% to 49.0%) and a relative constant CO_2 dry-basis purity (97.6 ± 0.2%) over more than 100-h testing under simulated natural gas flue gas separation conditions.

The separation performance of the NCIL membrane was also evaluated using simulated coal-fired flue gas. Figure 34 shows stable separation performance for 100 h with CO_2 dry-basis purity of 97.9 ± 0.1% and 97.5 ± 0.5% at 65 and 70°C, respectively. Given the practical and scalable fabrication of the NCIL membrane, this work presents a promising candidate for highly efficient CO_2 capture from various point sources.

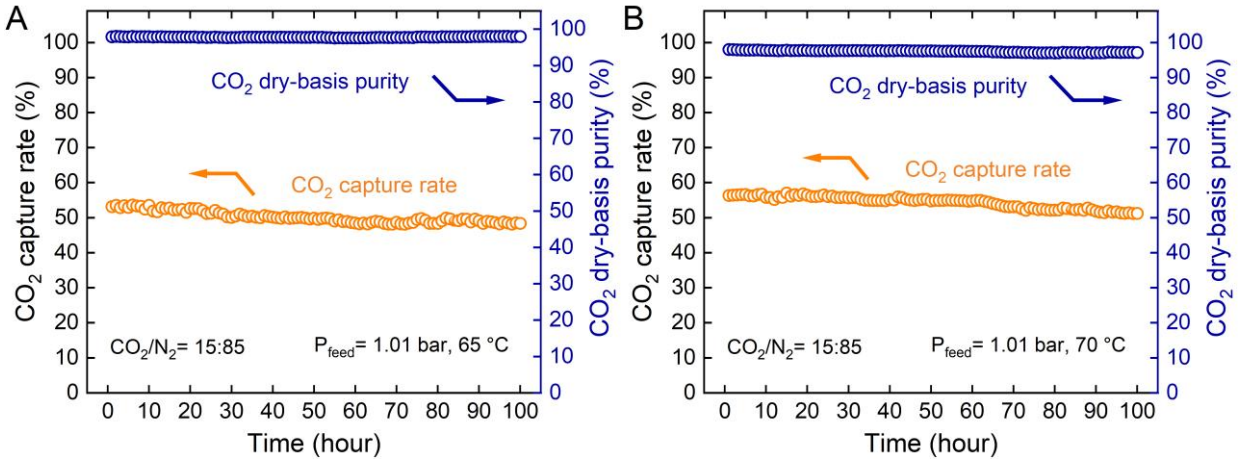

Figure 34. *Long-term stability results of the 75 cm^2 NCIL hollow fiber membranes for CO_2 capture from simulated coal-fired flue gas. (A) feed gas composed of 11.3 vol% CO_2, 25 vol% H_2O and balanced N_2 at 65°C and (B) feed gas composed of 10.5 vol% CO_2, 31.2 vol% H_2O and balanced N_2 at 70°C. Unless otherwise specified, the feed side pressure and permeate side pressure were controlled at 1.01 bara and 0.15 bara. The mixture gas introduced before humidifier was controlled at 200 sccm.*

In another test for a feed containing 4.5 vol% CO_2, 13.0 vol% H_2O, and 82.5 vol% N_2, water vapor was introduced to sweep the permeate side so the partial pressure of CO_2 was further decreased. Figure 35 shows both CO_2 purity (dry-basis) and CO_2 capture efficiency increased with increasing sweep H_2O/CO_2 ratio. A CO_2 capture efficiency of 81% was achieved at a permeate sweep H_2O/CO_2 ratio of 13. The membrane also showed good stability during a 60-h continuous testing at 65°C (Figure 36). The permeate CO_2 concentration (dry base) was>97.6% throughout the testing.

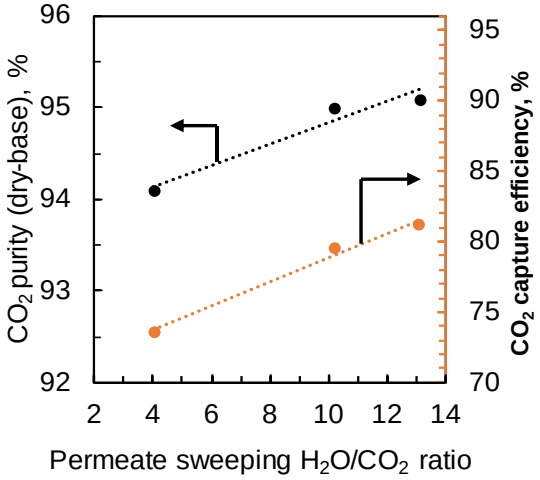

Figure 35. *Separation performance as a function of permeate sweep H_2O/CO_2 ratio.*

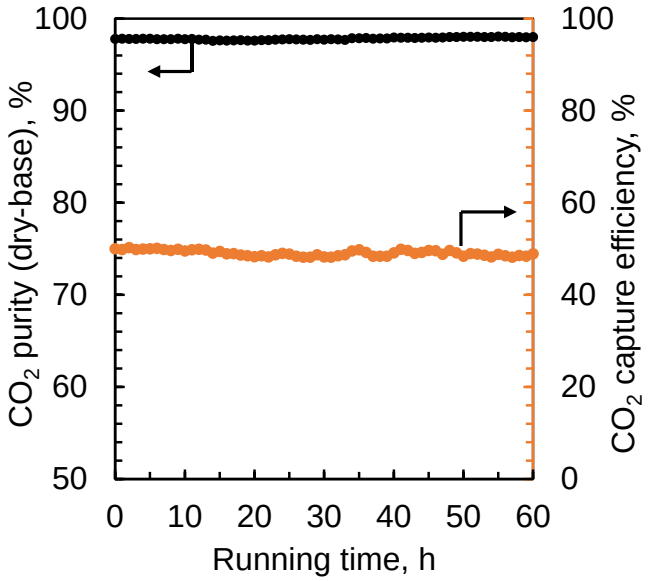

***Figure 36**. Membrane stability at 65°C.*

Note that during these tests, water vapor was introduced for sweeping in a co-current flow mode (H_2O vapor and flue gas flowed in the same direction). To further improve driving force for mass transfer, a counter-current flow mode (H_2O vapor and flue gas are in the opposite directions) were tested. For a feed containing 5.4 vol% CO_2, 9.6 vol% H_2O, and 85 vol% N_2, a CO_2 capture efficiency of 97.7% was achieved at 70°C with a CO_2 permeate concentration (dry-basis) of 96.6%.

The effects of feed gas flow rate, permeate side pressure, water sweeping rate, and water feed concentration on separation properties of the membrane were then sysmatically studied with reustls shown in Tables 3-6.

***Table 3**. Effect of feed gas flow rate on separation properties.*

Dry feed flow rate (sccm)*	CO_2 capture rate (%)	CO_2 Dry-basis purity (%)	CO_2 permeance (GPU)	CO_2/N_2 selectivity
100	94.1	92.2	990	760
150	95.5	95.0	1,750	1,430
200	91.2	96.2	1,860	1,440
250	85.4	96.6	1,820	1,450
300	81.3	96.7	1,840	1,400

*: Membrane was tested at 70°C for feed of 4.8% CO_2, 9.8% H_2O and balance N_2, 1.01 bara feed pressure and 0.1 bara permeate side pressure with 200 sccm water sweep rate in the permeate side.

***Table 4**. Effect of permeate side pressure on separation properties.*

Permeate pressure (bara)*	CO_2 capture rate (%)	CO_2 Dry-basis purity (%)	CO_2 permeance (GPU)	CO_2/N_2 selectivity
0.1	96.2	96.2	1,860	1,710
0.15	96.5	96.5	2,060	1,900
0.20	96.3	96.3	1,840	1,790

*: Membrane was tested at 70°C for feed of 4.8% CO_2, 9.8% H_2O and balance N_2, 1.01 bara feed pressure with 200 sccm dry feed flow rate and 200 sccm water sweep rate in the permeate side.

***Table 5**. Effect of water sweep rate on separation properties.*

Water sweep rate (sccm)*	CO_2 capture rate (%)	CO_2 Dry-basis purity (%)	CO_2 permeance (GPU)	CO_2/N_2 selectivity
0	29.2	80.2	290	270
22	70.5	95.2	1,570	1,350
58	77.3	95.5	1,700	1,410
89	87.9	96.1	1,850	1,780
200	91.2	96.2	1,860	1,710

*: Membrane was tested at 70°C for feed of 4.8% CO_2, 9.8% H_2O and balance N_2, 1.01 bara feed pressure and 0.1 bara permeate side pressure with 200 sccm dry feed flow rate.

***Table 6**. Effect of water feed concentration on separation properties.*

Water feed concentration (%)	CO_2 capture rate (%)	CO_2 Dry-basis purity (%)	CO_2 permeance (GPU)	CO_2/N_2 selectivity
0	91.2	96.2	1,860	1,710
15	93.3	96.7	2,280	2,030
20	93.4	97.0	2,480	2,380
25	92.9	97.2	2,560	2,590
31	93.0	97.0	2,740	2,500

*: Membrane was tested at 70°C for feed of 4.8% CO_2, 9.8% H_2O and balance N_2, 1.01 bara feed pressure and 0.1 bara permeate side pressure with 200 sccm dry feed flow rate and 200 sccm water sweep rate in the permeate side.

The stability of the 75 cm^2 hollow fiber NCIL membrane under water vapor mode was also investigated. Figure 37 shows the testing results using a 1.01 bara feed pressure and 0.1 bara permeate pressure with simulated NGCC flue gas (4.5 vol% CO_2, 9.8 vol% H_2O and 5.0 vol% O_2 and balanced N_2), CO_2 dry-basis purity maintained >95 vol% and CO_2 capture efficiency was >80% for the initial 100 hours. Then, the feed flow rate was decreased from 200 SCCM to 150 SCCM, resulting in an increase in CO_2 capture efficiency to 93%. This performance was sustained over the next 80 hours tested, demonstrating consistent separation efficiency and reasonable stability.

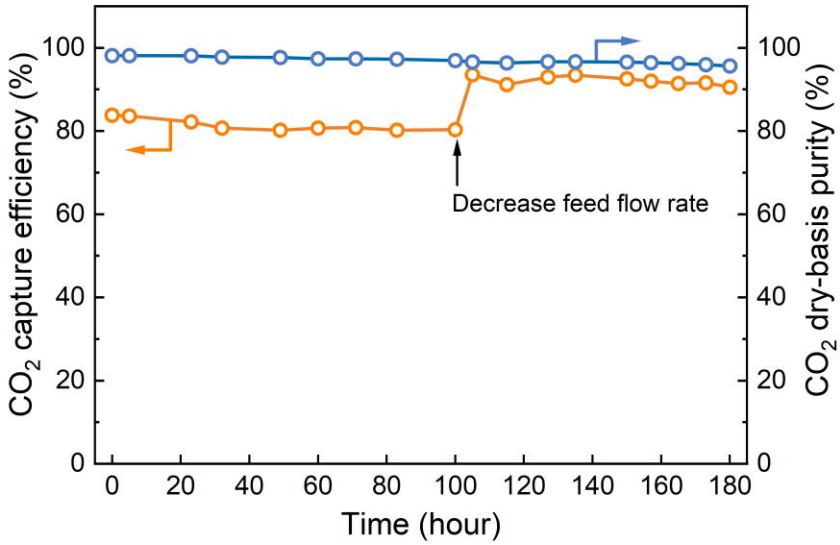

***Figure 37**. Long-term stability testing of a NCIL membrane.*

3.6. Gas Permeation Properties of the Dehydration Membranes

SPEEK membranes were fabricated by dissolving SPEEK into methanol solution with different concentrations. SPEEK membranes were scaled up from flat sheet to hollow fiber (HF) with membrane area around 10 cm^2. Various membrane substrates, including PES, PVDF, and modified polyether sulphone (mPES), with different molecular weight cutoffs, were screened during the process. The feed composition closely mirrored the permeate side gas composition of the NCIL membrane, consisting of 14.5 vol% H_2O and balanced CO_2. The operating temperature was 70ºC. The permeate side pressure was maintained at 0.2 bara.

As shown in Table 7, employing a substrate of lower molecular weight cutoffs (ranging from 50 kDa to 120 kDa) yielded either no water permeance (PES 75 kDa and PVDF 50 kDa) or very low water permeance (PES 120 kDa and PVDF 100 kDa). When selecting mPES as substrate for the membrane, a significant enhancement in membrane performance was observed. Following optimization of the feed flow rate and SPEEK solution in methanol, the highest H_2O permeance of 11,500 and H_2O/CO_2 selectivity of 1,000 were achieved. These results were obtained with a feed flow rate of 120 sccm and SPEEK solution in methanol of 2 wt%.

Table 7. *Testing results for SPEEK membranes.*

Membrane substrate	Permeate pressure (bara)	Feed flow rate (SCCM)	SPEEK solution in methanol (wt.%)	CO_2 flux ($mol \cdot s^{-1} \cdot m^{-2}$)	H_2O flux ($mol \cdot s^{-1} \cdot m^{-2}$)	H_2O permeance (GPU)	H_2O/ CO_2 selectivity
PES (75 kDa)	0.2	60	3.75	N/A	N/A	N/A	N/A
PVDF (50 kDa)	0.2	60	3.75	N/A	N/A	N/A	N/A
PES (120 kDa)	0.2	60	1.0	1.05E-06	2.11E-03	610	1,050
PVDF (100 kDa)	0.2	60	1.0	1.12E-06	1.94E-03	560	890
mPES (300 kDa)	0.2	60	5.0	1.86E-06	1.25E-02	5,870	6,220
	0.2	60	3.75	2.60E-06	1.20E-02	5,570	4,140
	0.2	120	3.75	9.30E-06	1.34E-02	6,500	1,300
	0.2	60	2.0	5.35E-06	1.42E-02	7,130	2,500
	0.2	120	2.0	2.16E-05	1.58E-02	11,300	980
	0.2	120	2.0	2.13E-05	1.6E-02	11,500	1,000

The membrane exhibited good stability during a 100-h continuous testing (Figure 38).

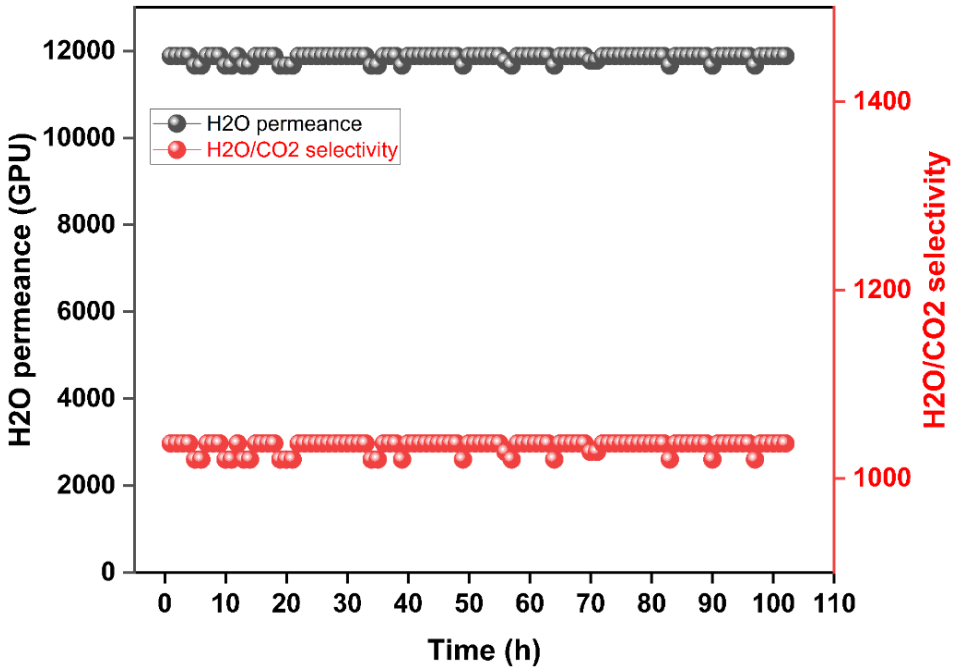

Figure 38*. Stability testing of SPEEK membrane for over 100 h at 70°C and 0.2 bara permeate pressure.*

3.7. Membrane Modeling Results

GTI Energy developed a standalone membrane model using the MATLAB platform. Table 8 compares modeling results with experimental data obtained from the 75 cm^2 NCIL membrane. The feed gas flow rate was 0.621 mol/h with a composition of 5.4 vol% CO_2, 85.0 vol% N_2 and 9.6 vol% H_2O. The sweep gas flow rate was 0.534 mol/h, consisting of 100 vol% H_2O. The comparison indicates that the retentate and permeate gas compositions, and the calculated CO_2 capture efficiency and CO_2 dry-basis purity closely align with the experimental results. This validates the accuracy of the membrane model.

Table 8. *Membrane model validation using experimental data.*

	Membrane modeling results (mole fraction)		**Experimental results (mole fraction)**	
Gases	**Retentate**	**Permeate**	**Retentate**	**Permeate**
CO_2	0.0010	0.0580	0.0010	0.0580
N_2	0.8994	0.0020	0.9000	0.0020
H_2O	0.0996	0.9400	0.0990	0.9400
CO_2 capture efficiency, %	98.00		97.56	
CO_2 dry basis purity, %	96.73		96.57	

The membrane model was then implemented through an integrated workflow involving Aspen Plus, Excel and MATLAB. The integrated platform was used to process flue gas from a ~650 MWe (net power) NGCC power plant. The flue gas flow rate was 138,406 kmol/h with a composition of 4.08 vol% CO_2, 74.3 vol% N_2, 8.75 vol% H_2O, 12.0 vol% O_2, and 0.89 vol% Ar. The sweep gas flow rate was 115,000 kmol/h, composed of 100 vol% H_2O. The simulation results are summarized in Table 9. Using a single-stage NCIL membrane system to treat this flue gas steam, the retentate gas composition was 0.12 vol% CO_2, 77.33 vol% N_2, 9.13 vol% H_2O, 12.49 vol% O_2 and 0.93 vol% Ar, while the permeate stream gas composition was 4.45 vol% CO_2, 0.185 vol% N_2, 95.24 vol% H_2O, 0.03 vol% O_2, and 0.002 vol% Ar. The membrane model calculated a CO_2 capture efficiency of 97.13% and a CO_2 dry-basis purity of 96.04%. To achieve this performance, a membrane area of approximately 1.5×10^6 m^2 would be required.

Table 9*. Simulation results for a ~650 MWe (net power) NGCC power plant flue gas treatment.*

Gases	**Retentate gas mole fractions**	**Permeate gas mole fractions**
CO_2	0.0012	0.0454
N_2	0.7733	0.00185
H_2O	0.0913	0.9524
O_2	0.1249	0.0003
Ar	0.0093	0.00002
CO_2 capture efficiency, %	97.13	
CO_2 dry basis purity, %	96.04	

3.8. Summary of the Techno-Economic Analysis

A detailed topical report on TEA was submitted to DOE with summary below:

3.8.1. Process description

An innovative water-vapor sweep and recycling process is designed to use the super high selectivity to achieve ≥95% CO_2 purity and ≥97% CO_2 capture efficiency by a single membrane stage for a typical NGCC flue gas feed. In this process, as shown in Figure 39, a blower is used to boost the cooled flue gas (stream 1) pressure from 1 bara to 1.5 bara (stream 2) before reaching the NCIL membrane. The water vapor (stream 8) is used to purge the permeate side of the NCIL membrane under a vacuum to provide sufficient driving force for the transport of CO_2. The treated flue gas (stream 3) is sent to the stack. The permeate from the NCIL membrane (stream 4, 0.15 bara) is slightly boosted to 0.35 bara (stream 5) and then sent to a highly H_2O-selective membrane, which also uses a vacuum on the permeate side (0.1 bara) to create the driving force for separating water vapor from CO_2. The retentate of the H_2O-selective membrane (stream 9) is compressed to 1 bara (stream 10) and water will be collected from the knockout vessel. The non-condensable stream (stream 11) is compressed in stages to 2,215 psia and sent for sequestration. The water collected from the knockout vessel is sent to a water boiler where the hot NGCC flue gas vaporizes the water to supply the necessary makeup water vapor (stream 13). The permeate from the water membrane (stream 6) is slightly boosted to 0.15 bara (steam 7) and then combined with stream 13 to form stream 8 for sweeping the NCIL membrane.

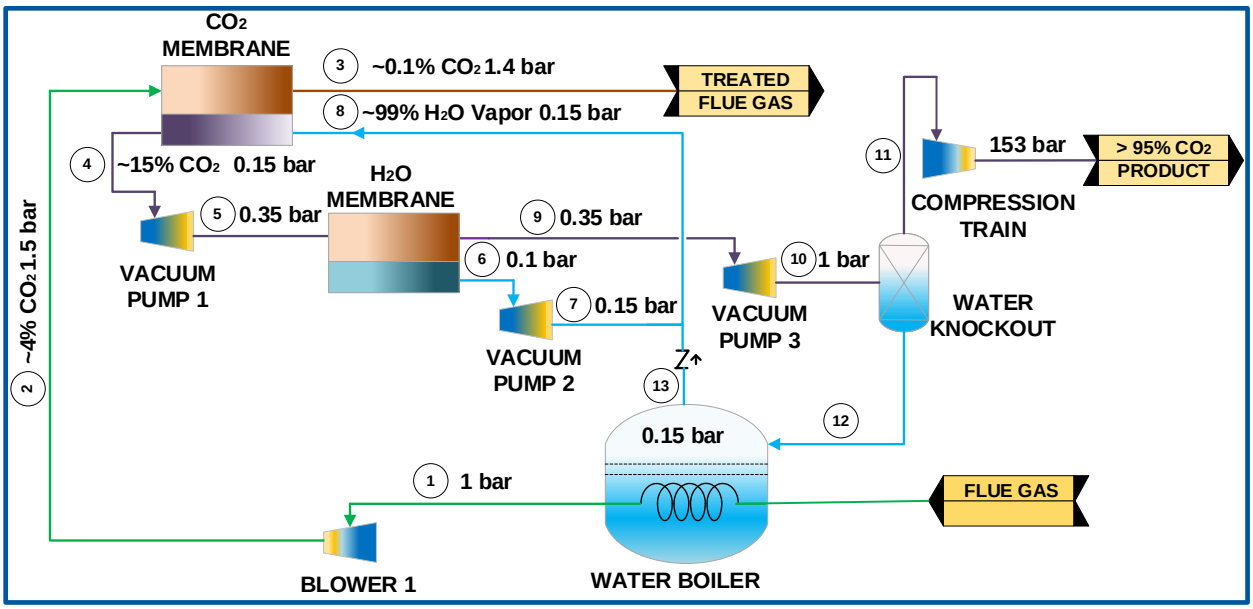

***Figure 39**. Flow diagram of an innovative NCIL membrane processes to achieve ≥97% CO_2 capture.*

3.8.2. Capital Cost Summary

The summary of the purchased equipment costs is shown in Table 10, which includes the breakdown of costs per process section and equipment.

***Table 10**. Capital cost summary of the NCIL membrane process.*

Equipment	Process Area	Purchased Equipment Cost, MM$ (2018)	Fraction of Area Cost	Fraction of Total Plant PEC
CO_2 Capture		**$123.3**		**79.5%**
Blower1 and EX-1	Flue Gas Compression	$7.0	5.7%	4.5%
CO_2 Membrane	NCIL CO_2 Selective Membrane Unit	$52.5	42.6%	33.8%
Vacuum 1	NCIL CO_2 Selective Membrane Unit, Permeate	$6.8	5.5%	4.4%
H_2O Membrane	H_2O Selective Membrane Unit	$49.7	40.3%	32.0%
Vacuum 2 and EX-2	H_2O Selective Membrane Unit, Permeate	$2.9	2.3%	1.9%
Vacuum 3 and EX-3	H_2O Selective Membrane Unit, Retentate	$4.2	3.4%	2.7%
Heat Exchanger/ Boiler	Make Up Vapor Generation	$0.2	0.2%	0.1%
CO_2 Compression		**$31.8**		**20.5%**
CO_2 Fan	Multi-Stage CO_2 Compression	$3.7	11.6%	2.4%
CO_2 Compression Train	Multi-Stage CO_2 Compression	$28.2	88.4%	18.2%
Total PEC		**$155.1**		

Table 10 presents the equipment costs and their percentage of the total PEC. The largest spending contributors are the CO_2 and H_2O membrane cost (65.8% of the total PEC), the compression of the CO_2 product (18.2% of the total PEC), and the flue gas compression (4.5% of the PEC). In total, these top three-line items represent more than 88% of the total PEC, and the membrane cost contributes more than 74% of that. Therefore, the membrane system, including NCIL and water-selective membrane units, is the main cost required for CO_2 capture.

Table 11 compares the TPC of the NCIL membrane process with DOE Case B31B.97. The cost of the CO_2 capture system includes compressing of the inlet gas, membrane separation, and other utilities. Compared with Case B31B.97, the NCIL membrane process shows a decrease in total plant cost of 26.5%.

***Table 11**. Comparison of TPC: NETL Case B31B.97 vs. the NCIL membrane process.*

(MM$ 2018)	NETL Rev4a Baseline Case B31B.97	NCIL Process
CO_2 Removal System	$442	$297
CO_2 Compression and Drying	$63	$74
Total	$505	$371
Difference		-26.5%

3.8.3. Operation and Maintenance Cost Summary

The comparison of the O&M costs between Case B31B.97 and the NCIL membrane process is shown in Table 12. The variable O&M costs show that the cost to replace the membranes is slightly higher than the cost to replace the solvent. The reduced fixed operating cost is due to the lower capital cost for the NCIL membrane process in comparison to Case B31B.97.

***Table 12**. Comparison of O&M Costs for the NCIL membrane process with DOE Case B31B.97.*

(MM$ 2018)	**NETL Rev4a Baseline Case B31B.97**	**NCIL Process**
Total Annual Fixed O&M	$36.42	$31.70
Total Annual Variable O&M	$20.00	$24.16
Annual Fuel	$152.16	$152.16

3.8.4. Operation and Maintenance Cost Summary

The LCOE and cost of CO_2 capture for all cases are shown in Table 13. The FOA included an estimated transportation, storage, and monitoring cost of $10/tonne of CO_2 captured and is the same for all the cases.

***Table 13**. LCOE and cost of capture summary.*

	Unit	**NETL. Rev 4a Case B31A**	**NETL. Rev 4a Case B31B.97**	**NCIL Process**
LCOE Excluding T&S	**$/MWh**	**$43.3**	**$66.1**	**$ 60.7**
Incremental Cost of CO_2 Capture	$/MWh	-	$22.8	$ 17.4
Increase in COE vs. Case B31A	%	-	**52.7%**	**40.3%**
Cost of CO_2 Capture	**$/tonne**	**-**	**$60.2**	**$47.8**

The cost of capture metric is further summarized with the savings seen by category between Case B31B.97 and the NCIL membrane process. Table 14 shows the breakdown of cost per costing category (i.e., capital, fixed, variable, and fuel costs).

***Table 14**. Cost of capture - contributions by cost category.*

CO_2 Capture Cost Breakdown	**Unit**	**NETL. Rev 4a Case B31B.97**	**NCIL Process**	**Saving vs. Case B31B.97**	**Fraction of Saving Over B31B.97**
Capital	$/tonne	$32.2	$23.4	$8.8	27%
Fixed	$/tonne	$10.8	$7.8	$3.0	28%
Variable	$/tonne	$6.6	$8.8	-$2.2	-33%
Fuel	$/tonne	$10.6	$7.8	$2.8	26%
Total	**$/tonne**	**$60.2**	**$47.8**	$12.4	21%

The calculated LCOE for the NCIL process is ~8% lower than Case B31B.97 ($60.7/MWh vs. $66.1/MWh). The lower LCOE can be attributed to the lower capital costs and fixed O&M costs for the membrane process. The CO_2 capture cost of the NCIL membrane process is $47.8/tonne. Compared with Case B31B.97, the CO_2 capture cost is reduced by ~21%. The reduction in capital cost makes the most contribution (71%) to the overall saving. Figure 40 shows a visual comparison of the cases and the cost categories.

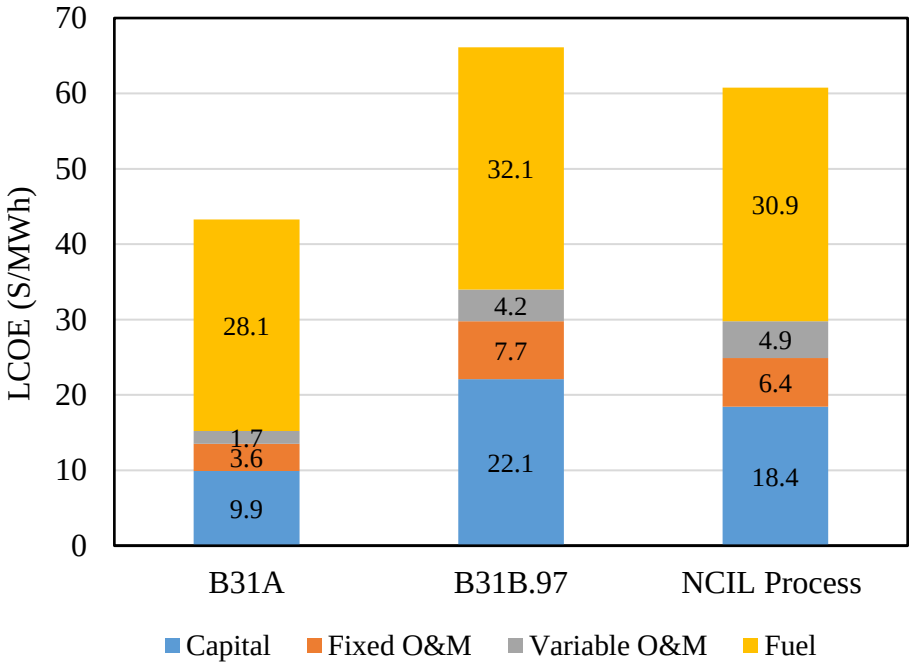

***Figure 40**. Comparison of LCOE for DOE Cases B31A, B31B.97, and the NCIL membrane process.*

4. Summary and Future Steps

A transformational process based on nano-confined ionic liquid membranes was developed for capturing ≥97% CO_2 from a NGCC flue gas with a target of a 40% reduction in the cost of CO_2 capture versus a DOE reference NGCC power plant for the same carbon capture efficiency.

NCIL membranes were prepared by loading amino acid ionic liquid into a framework composed of single-walled carbon nanotube mesh filled with graphene oxide quantum dots. The nano-confined space between SWCNTs, combined with nanometer-sized GOQDs with rich oxygen-containing functional groups, stabilizes the amino acid ILs with amine groups during membrane operations. The membranes exhibited CO_2 permeance as high as 2,000 GPU with a CO_2/N_2 selectivity of 2,300 for a typical NGCC flue gas composition.

When water vapor sweep was applied in the permeate side and a counter-current flow mode was used, 96.6% CO_2 dry-basis purity and 97.6% CO_2 capture rate were achieved for a simulated NGCC flue gas with single stage.

Highly H_2O-selective sulfonated poly(ether ether ketone) membranes were successfully developed for recovering H_2O vapor. These membranes exhibited H_2O permeance great than 11,000 GPU and H_2O/CO_2 selectivity greater than 1,000 at 70ºC for a feed mixture consisting of 14.5 vol% CO_2 and balanced H_2O.

A standalone membrane model using MATLAB platform was developed to estimate the permeation of a multi-component gas mixture, containing N_2, CO_2, and H_2O, through a membrane module. The model was validated with experimental data.

Techno-economic analysis based on testing data collected suggests the transformational membrane process can achieve 97% CO_2 capture efficiency with a cost of $47.8/tonne of CO_2, which is a 21% reduction versus DOE's reference case B31B.97.

The next phase would be a bench-scale development including the following:

- Scaleup of membrane to commercial-sized modules;
- Integrate basic technology components (NCIL and dehydration membranes) in lab and validate they can work together as designed;
- Design and construct a 1 tonne per day (1 TPD) bench-scale system;
- Perform parametric tests and ≥200 hours steady state operation with actual flue gas for the 1 TPD system; and
- Perform TEA and sensitivity studies and determine operating conditions for low-cost CO_2 production

References

[1] DOE/NETL. *Carbon Capture Program R&D Compendium of Carbon Capture Technology*; 2020.

[2] K. Pulidindi, H. Pandey, Dimethyl carbonate market size by application (polycarbonate, solvent, Bioimaging, Sensors, Catalysis and Photovoltaic Devices. *Chem. Commun. 48* (31), 3686–3699 (2012).

[3] H. P. Cong, J. F. Chen, S. H. Yu, Graphene-Based Macroscopic Assemblies and Architectures: An Emerging Material System. *Chem. Soc. Rev., 43* (21), 7295–7325 (2014).

[4] M. Nurunnabi, Z. Khatun, K. M. Huh, S. Y. Park, D. Y. Lee, K. J. Cho, Y. Lee, In Vivo Biodistribution and Toxicology of Carboxylated Graphene Quantum Dots. *ACS Nano, 7* (8), 6858–6867 (2013).

[5] C. Wu, C. Wang, T. Han, X. Zhou S. Guo, J. Zhang, Insight into the Cellular Internalization and Cytotoxicity of Graphene Quantum Dots. *Adv. Healthc. Mater. 2* (12), 1613–1619 (2013).

[6] M. Fathizadeh, H. N. Tien, K. Khivantsev, Z. Zong, F. Zhou, M. Yu, Polyamide/Nitrogen-Doped Graphene Oxide Quantum Dots (N-GOQD) Thin Film Nanocomposite Reverse Osmosis Membranes for High Flux Desalination. *Desalination, 451*, 125–132 (2019).

[7] R. E. James, D. Kearins, M. Turner, M. Woods, N. Kuehn, A. Zoelle, *Cost and Performance Baseline for Fossil Energy Plants Volume 1: Bituminous Coal and Natural Gas to Electricity*; NETL, 2019.

[8] D. T. Coker, B. D. Freeman, G. K. Fleming, Modeling multicomponent gas separation using hollow-fiber membrane contactors. *AIChE Journal*, 44, 6 (1998).

[9] K. Kneifel, S. Nowak, W. Albrecht, R. Hilke, R. Just, K. V. Peinemann, Hollow Fiber Membrane Contactor for Air Humidity Control: Modules and Membranes. *J. Memb. Sci. 276* (1–2), 241–251 (2006).

[10] K. L. Wang, S. H. McCray, D. D. Newbold, E. L. Cussler, Hollow Fiber Air Drying. *J. Memb. Sci., 72* (3), 231–244 (1992).

[11] I. Blume, P. J. F. Schwering, M. H. Mulder, C.A. Smolders, Vapour Sorption and Permeation Properties of Poly (Dimethylsiloxane) Films. *J. Memb. Sci., 61*, 85–97 (1991).

[12] L. Jia, X. Xu, H. Zhang, J. Xu, Permeation of Nitrogen and Water Vapor through Sulfonated Polyetherethersulfone Membrane. *J. Polym. Sci. Part B Polym. Phys. 35* (13), 2133 (1997).

[13] S. J. Metz, W. J. C Van De Ven, M. H. V. Mulder, M. Wessling, Mixed Gas Water Vapor/N_2 Transport in Poly (Ethylene Oxide) Poly (Butylene Terephthalate) Block Copolymers. *J. Memb. Sci., 266* (1–2), 51–61 (2005).

[14] S. J. Metz, W. J. C. Van de Ven, J. Potreck, M. H. V. Mulder, M. Wessling, Transport of Water Vapor and Inert Gas Mixtures through Highly Selective and Highly Permeable Polymer Membranes. *J. Memb. Sci., 251* (1–2), 29–41 (2005).

[15] S. P. Nunes, K. V. Peinemann, *Membrane Technology*; Wiley Online Library, 2001.

[16] H. Sijbesma, K. Nymeijer, R. van Marwijk, R. Heijboer, J. Potreck, M. Wessling, Flue Gas Dehydration Using Polymer Membranes. *J. Memb. Sci., 313* (1–2), 263–276 (2008).

[17] D. T. Coker and B. D. Freeman, G. K. Fleming., Modeling multicomponent gas separation using hollow-fiber membrane contactors. *AIChE Journal*, 44, 6 (1998).

[18] Y. Han, W.S. Ho. Design of amine-containing CO_2-selective membrane process for carbon capture from flue gas. *Industrial & Engineering Chemistry Research*, 59, 5340-5350 (2020).

[19] DOE/NETL, "Cost and Performance Baseline for Fossil Energy Plants Volume 1: Bituminous Coal and Natural Gas to Electricity, Revision 4a", U.S. Department of Energy, Washington D.C., 2022.

[20] Z. Sheng, J. Zhang, J. Liu, Y. Zhang, X. Chen, X. Hou, Liquid-based porous membranes. *Chem. Soc. Rev.* 49, 7907–7928 (2020).

[21] S. Zhang, H. Li, H. Li, B. Sengupta, S. Zha, S. Li, M. Yu, Negative Charge Confined Amine Carriers within the Nanowire Network for Stable and Efficient Membrane Carbon Capture. *Adv. Funct. Mater.* 30, 1–7 (2020).

[22] K. E. Gutowski, E. J. Maginn, Amine-functionalized task-specific ionic liquids: A mechanistic explanation for the dramatic increase in viscosity upon complexation with CO_2 from molecular simulation. *J. Am. Chem. Soc.* 130, 14690–14704 (2008).

[23] B. Sengupta, Q. Dong, R. Khadka, D. K. Behera, R. Yang, J. Liu, J. Jiang, P. Keblinski, G. Belfort, M. Yu, Carbon-doped metal oxide interfacial nanofilms for ultrafast and precise separation of molecules. *Science* 381, 1098–1104 (2023).

[24] W. R. Bowen, J. S. Welfoot, Modelling of membrane nanofiltration—pore size distribution effects. *Chem. Eng. Sci.* 57, 1393–1407 (2002).

[25] M. Althuluth, J. P. Overbeek, H. J. van Wees, L. F. Zubeir, W. G. Haije, A. Berrouk, C. J. Peters, M. C. Kroon, Natural gas purification using supported ionic liquid membrane. *J. Membr. Sci.* 484, 80–86 (2015).

[26] Y. Wu, X. Ma, Y. Li, W. Guan, J. Tong, N. Hu, Theoretical and experimental determination of the number of water molecules breaking the structure of a glycine-based ionic liquid. *RSC Adv.* 4, 10531–10541 (2014).

[27] B. Comesaña-Gándara, J. Chen, C. G. Bezzu, M. Carta, I. Rose, M.-C. Ferrari, E. Esposito, A. Fuoco, J. C. Jansen, N. B. McKeown, Redefining the Robeson upper bounds for CO_2/CH_4 and CO_2/N_2 separations using a series of ultrapermeable benzotriptycene-based polymers of intrinsic microporosity. *Energy Environ. Sci.* 12, 2733–2740 (2019).

[28] L. M. Robeson, The upper bound revisited. *J. Membr. Sci.* 320, 390–400 (2008).

[29] S. Zhao, Z. Zhao, Z. Zha, Z. Jiang, Z. Wang, M. D. Guiver, Amine-Rich Molecular Nodule-Assembled Membrane Having 5 Angstrom Channels for CO_2/N_2 Separation. *Adv. Funct. Mater.* 34, 1–9 (2024).

[30] D. Li, R. Wang, T. S. Chung, Fabrication of lab-scale hollow fiber membrane modules with high packing density. *Sep. Purif. Technol.* 40, 15–30 (2004).

[31] S. Karan, Z. Jiang, A. G. Livingston, Sub–10 nm polyamide nanofilms with ultrafast solvent transport for molecular separation. *Science* 348, 1347–1351 (2015).

[32] Y. Jin, Q. Song, N. Xie, W. Zheng, J. Wang, J. Zhu, Y. Zhang, Amidoxime-functionalized polymer of intrinsic microporosity (AOPIM-1)-based thin film composite membranes with

ultrahigh permeance for organic solvent nanofiltration. *J. Membr. Sci.* 632, 119375 (2021).

[33] Q. Lan, C. Feng, K. Ou, Z. Wang, Y. Wang, T. Liu, Phenolic membranes with tunable sub-10-nm pores for nanofiltration and. *J. Membr. Sci.* 640, 119858 (2021).

[34] Q. Yang, Y. Su, C. Chi, C. T. Cherian, K. Huang, V. G. Kravets, F. C. Wang, J. C. Zhang, A. Pratt, A. N. Grigorenko, F. Guinea, A. K. Geim, R. R. Nair, Ultrathin graphene-based membrane with precise molecular sieving and ultrafast solvent permeation. *Nat. Mater.* 16, 1198–1202 (2017).

[35] L. Huang, J. Chen, T. Gao, M. Zhang, Y. Li, L. Dai, L. Qu, G. Shi, Reduced Graphene Oxide Membranes for Ultrafast Organic Solvent Nanofiltration. *Adv. Mater.* 28, 8669–8674 (2016).

[36] L. Shen, Q. Shi, S. Zhang, J. Gao, D. C. Cheng, M. Yi, R. Song, L. Wang, J. Jiang, R. Karnik, S. Zhang, Highly porous nanofiber-supported monolayer graphene membranes for ultrafast organic solvent nanofiltration. *Sci. Adv.* 7, 6263 (2025).

[37] W. Chen, Z. Zhang, C. Yang, J. Liu, H. Shen, K. Yang, Z. Wang, PIM-based mixed-matrix membranes containing MOF-801/ionic liquid nanocomposites for enhanced CO_2 separation performance. *J. Membr. Sci.* 636, 119581 (2021).

[38] Y. Ban, Z. Li, Y. Li, Y. Peng, H. Jin, W. Jiao, A. Guo, P. Wang, Q. Yang, C. Zhong, W. Yang, Confinement of Ionic Liquids in Nanocages: Tailoring the Molecular Sieving Properties of ZIF-8 for Membrane-Based CO_2 Capture . *Angew. Chemie* 127, 15703 (2015).

[39] H. Lin, K. Gong, P. Hykys, D. Chen, W. Ying, Z. Sofer, Y. Yan, Z. Li, X. Peng, Nanoconfined deep eutectic solvent in laminated MXene for efficient CO_2 separation. *Chem. Eng. J.* 405, 126961 (2021).

[40] W. Ying, J. Cai, K. Zhou, D. Chen, Y. Ying, Y. Guo, X. Kong, Z. Xu, X. Peng, Ionic Liquid Selectively Facilitates CO_2 Transport through Graphene Oxide Membrane. *ACS Nano* 12, 5385–5393 (2018).

[41] M. Karunakaran, L. F. Villalobos, M. Kumar, R. Shevate, F. H. Akhtar, K. V. Peinemann, Graphene oxide doped ionic liquid ultrathin composite membranes for efficient CO_2 capture. *J. Mater. Chem. A* 5, 649–656 (2017).

[42] X. Wan, X. Wang, T. Wan, Y. Yan, Z. Ye, X. Peng, Bio-inspired ferromagnetic graphene oxide/magnetic ionic liquid membrane for highly efficient CO_2 separation. *Appl. Mater. Today* 24, 101164 (2021).

[43] D. Chen, W. Wang, W. Ying, Y. Guo, D. Meng, Y. Yan, R. Yan, X. Peng, CO_2-philic WS_2 laminated membranes with a nanoconfined ionic liquid. *J. Mater. Chem. A* 6, 16566–16573 (2018).

[44] D. Chen, W. Ying, Y. Guo, Y. Ying, X. Peng, Enhanced Gas Separation through Nanoconfined Ionic Liquid in Laminated MoS_2 Membrane. *ACS Appl. Mater. Interfaces* 9, 44251–44257 (2017).

[45] W. Guo, S. M. Mahurin, R. R. Unocic, H. Luo, S. Dai, Broadening the Gas Separation Utility of Monolayer Nanoporous Graphene Membranes by an Ionic Liquid Gating. *Nano Lett.* 20, 7995–8000 (2020).

[46] J. Albo, T. Tsuru, Thin ionic liquid membranes based on inorganic supports with different

pore sizes. *Ind. Eng. Chem. Res.* 53, 8045–8056 (2014).

[47] X. M. Zhang, Z. H. Tu, H. Li, L. Li, Y. T. Wu, X. B. Hu, Supported protic-ionic-liquid membranes with facilitated transport mechanism for the selective separation of CO_2. *J. Membr. Sci.* 527, 60–67 (2017).

[48] S. M. Mahurin, J. S. Lee, G. A. Baker, H. Luo, S. Dai, Performance of nitrile-containing anions in task-specific ionic liquids for improved CO_2/N_2 separation. *J. Membr. Sci.* 353, 177–183 (2010).

[49] M. Y. Abdelrahim, C. F. Martins, L. A. Neves, C. Capasso, C. T. Supuran, I. M. Coelhoso, J. G. Crespo, M. Barboiu, Supported ionic liquid membranes immobilized with carbonic anhydrases for CO_2 transport at high temperatures. *J. Membr. Sci.* 528, 225–230 (2017).

[50] E. Santos, J. Albo, A. Irabien, Acetate based Supported Ionic Liquid Membranes (SILMs) for CO_2 separation: Influence of the temperature. *J. Membr. Sci.* 452, 277–283 (2014).

[51] J. Yin, C. Zhang, Y. Yu, T. Hao, H. Wang, X. Ding, J. Meng, Tuning the microstructure of crosslinked Poly(ionic liquid) membranes and gels via a multicomponent reaction for improved CO_2 capture performance. *J. Membr. Sci.* 593, 117405 (2020).

[52] J. Zhou, M. M. Mok, M. G. Cowan, W. M. Mcdanel, T. K. Carlisle, D. L. Gin, R. D. Noble, High-Permeance Room-Temperature Ionic-Liquid-Based Membranes for CO_2/N_2 Separation. *Ind. Eng. Chem. Res.* 53, 20064–20067 (2014)

[53] J. Y. Lim, J. K. Kim, C. S. Lee, J. M. Lee, J. H. Kim, Hybrid membranes of nanostructrual copolymer and ionic liquid for carbon dioxide capture. *Chem. Eng. J.* 322, 254–262 (2017).

[54] S. Janakiram, L. Ansaloni, S. A. Jin, X. Yu, Z. Dai, R. J. Spontak, L. Deng, Humidity-responsive molecular gate-opening mechanism for gas separation in ultraselective nanocellulose/IL hybrid membranes. *Green Chem.* 22, 3546–3557 (2020).

[55] V. A. Kusuma, M. K. Macala, J. Liu, A. M. Marti, R. J. Hirsch, L. J. Hill, D. Hopkinson, Ionic liquid compatibility in polyethylene oxide/siloxane ion gel membranes. *J. Membr. Sci.* 545, 292–300 (2018).

[56] H. Li, F. Wang, H. Li, B. Sengupta, D. K. Behera, S. Li, M. Yu, Ultra-selective membrane composed of charge-stabilized fixed carrier and amino acid-based ionic liquid mobile carrier for highly efficient carbon capture. *Chem. Eng. J.* 453, 139780 (2023).

[57] D. K. Behera, F. Wang, B. Sengupta, K. Friedman, S. Li, M. Yu, A facilitated transport membrane composed of amine-containing ionic liquid confined in a GO/CNT network for highly efficient carbon capture. *J. Membr. Sci.* 712, 123177 (2024).

[58] X. Xu, J. Dong, X. Xiao, X. Zhao, Q. Zhang, Constructing Thin and Cross-Linked Polyimide Membranes by Interfacial Reaction for Efficient CO_2 Separation. *ACS Sustain. Chem. Eng.* 9, 5546–5556 (2021).

[59] J. M. P. Scofield, P. A. Gurr, J. Kim, Q. Fu, S. E. Kentish, G. G. Qiao, Development of novel fluorinated additives for high performance CO_2 separation thin-film composite membranes. *J. Membr. Sci.* 499, 191–200 (2016).

[60] L. S. White, K. D. Amo, T. Wu, T. C. Merkel, Extended field trials of Polaris sweep modules for carbon capture. *J. Membr. Sci.* 542, 217–225 (2017).

Appendices

Table S1. *Comparison of porosity over tortuosity factor (ε/τ) of nano-structure (NS) membranes.*

Confinement type	Confinement materials	Confined pore or channel size (nm)	Ionic liquid	Temperature (K)	CO_2 permeance (GPU)	CO_2/N_2 selectivity	Membrane thickness	Reference
Nanocage	MOF-801	0.7	[Bmim][NTf_2]	308	380	29	25 μm	[37]
	ZIF-8*	0.6	[Bmim][Tf_2N]	303	16	116	30 μm	[38]
Nanochannel	$Ti_3C_2T_x$*	1.5	1ChCl-4EG	293	26	320	2 μm	[39]
	GO	1.9	[Bmim][BF_4]	323	68	380	1 μm	[40]
	GO	1.1	[Emim][Ac]	298	37	130	400 nm	[41]
	GO*	1.3	[$P_{6,6,6,14}$][$FeCl_4$]	298	83	180	45 nm	[42]
	WS_2	1.2	[Bmim][BF_4]	298	50	150	150 nm	[43]
	MoS_2*	1.2	[Bmim][BF_4]	298	48	130	740 nm	[44]
Nanopore	Nano-porous Graphene	1 .0	[Bmim][BF_4]	295	4,000	32	400 nm	[45]
	TiO_2	2.5	[Emim][Ac]	298	68	34	780 nm	[46]
	CNT*	9.8	[Emim][Gly]	343	1,700	1,100	560 nm	This work

***** Permeation test of the CNT mesh coated PES membrane was conducted under 0.5 bara feed side pressure.

Table S2. *Comparison of CO_2 separation performance of the nanoconfined IL membranes reported in the literature.*

Confinement type	Confinement materials	Confined pore or channel size (nm)	Ionic liquid	Temperature (K)	CO_2 permeance (GPU)	CO_2/N_2 selectivity	Membrane thickness	Reference
Nanocage	MOF-801	0.7	[Bmim][NTf_2]	308	380	29	25 μm	[37]
	ZIF-8*	0.6	[Bmim][Tf_2N]	303	16	116	30 μm	[38]
Nanochannel	$Ti_3C_2T_x$*	1.5	1ChCl-4EG	293	26	320	2 μm	[39]
	GO	1.9	[Bmim][BF_4]	323	68	380	1 μm	[40]
	GO	1.1	[Emim][Ac]	298	37	130	400 nm	[41]
	GO*	1.3	[$P_{6,6,6,14}$][$FeCl_4$]	298	83	180	45 nm	[42]
	WS_2	1.2	[Bmim][BF_4]	298	50	150	150 nm	[43]
	MoS_2*	1.2	[Bmim][BF_4]	298	48	130	740 nm	[44]
Nanopore	Nano-porous Graphene	1 .0	[Bmim][BF_4]	295	4,000	32	400 nm	[45]
	TiO_2	2.5	[Emim][Ac]	298	68	34	780 nm	[46]
	CNT*	9.8	[Emim][Gly]	343	1,700	1,100	560 nm	This work

***** Membrane separation performance was tested using CO_2 and N_2 gas mixture. GPU: gas permeation unit; 1 GPU= 3.35×10^{-10} mol $(m^2\cdot s\cdot Pa)^{-1}$.

Table S3. *Comparison of CO_2 separation performance of the IL-based membranes reported in the literature.*

Membrane type	Support	Ionic liquid	Temperature (K)	CO_2 permeance (GPU)	CO_2/N_2 selectivity	Membrane thickness	Reference
SILMs	PES	[DMAPAH][TFA]	303	13	90	120 μm	[47]
		[Emim][$B(CN)_4$]	298	34	53	60 μm	[48]
	PVDF	[C_4mim][NTf_2]	373	5.8	36	125 μm	[49]
		[Vbtma][Ac]	298	8.8	39	125 μm	[50]
PILMs	Poly[Emim][$C(CN)_3$]/[Emim][$C(CN)_3$]		293	3.6	64	120 μm	[51]
	Poly[VHLM][Tf_2N]/[Emim][Tf_2N]		298	6,400	25	100 nm	[52]
ILCMs	SBS-g-POEM/[Emim][DCA]		308	4.6	25	100 μm	[53]
	NF cellulose/[Emim][Ac]*		308	5.5	370	60 μm	[54]
	PEO/[P_{1444}][Tf_2N]		313	1.3	24	230 μm	[55]
FTILMs*	CNT-PSS/[Emim][Gly]		343	1,300	750	235 nm	[56]
	CNT-GO/[Emim][Gly]			1,600	400	230 nm	[57]
	CNT/[Emim][Gly]			1,700	1,100	560 nm	This work

† Membrane type abbreviation: Supported ionic liquid membranes (SILMs), Poly(ionic liquid) membranes (PILMs), Ionic liquid composite membranes (ILCMs), Facilitated transport ionic liquid membranes (FTILMs).

***** Membrane separation performance was tested using CO_2 and N_2 gas mixture. GPU: gas permeation unit; 1 GPU= 3.35×10^{-10} mol $(m^2\cdot s\cdot Pa)^{-1}$.

Table S4. *Comparison of CO_2 separation performance of conventional thin film polymeric and facilitated transport membranes reported in the literatures.*

Membrane type†	Membrane description	Temperature (K)	CO_2 permeance (GPU)	CO_2/N_2 selectivity	Membrane thickness	Reference
PMs	PI	308	300	36	103 nm	[58]
	PEG-b-PPFPA	308	1,830	17	870 nm	[59]
	Polaris 2nd Gen*	303	1,670	50	100 nm	[60]
FTMs*	PVAm/K-Gly	330	900	173	350 nm	[61]
	PVAm (Pilot)	318	260	300	1.2 μm	[62]
	PVAm/PDA	298	1,900	83	165 nm	[63]
	TMC/DNMDAm/DGBAmE	295	1,600	140	500 nm	[64]
	PNVF-co-Vam/PZEA-Sar (Pilot)	340	1,450	190	170 nm	[65]
LFTMs*	CNT/PSS/PEI	353	820	460	230 nm	[66]
	GO/EDA	348	660	572	28 nm	[67]
	CNT/PSS/TEPA	353	1,300	450	220 nm	[21]
	CNT/[Emim][Gly]	343	1,700	1,100	560 nm	This work

† Membrane type abbreviation: Polymeric membranes (PMs), Facilitated transport membranes (FTMs), Liquid-based facilitated transport membranes (LFTMs).

***** Membrane separation performance was tested using CO_2 and N_2 gas mixture. GPU: gas permeation unit; 1 GPU= 3.35×10^{-10} mol $(m^2\cdot s\cdot Pa)^{-1}$.

List of Acronyms

AAIL: amino acid ionic liquid
B31B.97: DOE baseline Case B31B with 97% CO_2 capture efficiency
BFD: block flow diagram
CNT: carbon nanotube
COE: cost of electricity
D.I. water: deionized water
DOE: U.S. Department of Energy
EDS: Energy-Dispersive Spectroscopy
EX: heat exchanger
FIB-SEM: Focused Ion Beam Scanning Electron Microscope
FOA: funding opportunity announcement
FTILMs: facilitated transport ionic liquid membranes
FTIR: Fourier Transform Infrared Spectroscopy
FTMs: facilitated transport membranes
GC: gas chromatography
GOQDs: graphene oxide quantum dots
GTI: GTI Energy
GPC: Gel Permeation Chromatography
GPU: gas permeation unit
HF: hollow fiber
LFTMs: liquid-based facilitated transport membranes
IL: ionic liquid
ILCMs: ionic liquid composite membranes
LCOE: levelized cost of electricity
MATLAB: Matrix Laboratory
MFC: mass flow controller
mPES: modified polyether sulphone
mol%: mole percentage
MTR: Membrane Technology and Research, Inc.
MWCO: weight cut-off
MW_e: megawatts of electrical power
NCIL: nano-confined ionic liquid
NETL: National Energy Technology Laboratory
NGCC: Natural gas combined cycle
NS: nano-structure

O&M: operating and maintenance
OSU: The Ohio State University
PEBAX: polyether block amide
PEC: purchased equipment cost
PEEK: poly(ether ether ketone)
PEG: polyethylene glycol
PEO: polyethylene oxide
PES: polyether sulfone
PILMs: poly(ionic liquid) membranes
PMs: polymeric membranes
PVDF: polyvinylidene fluoride
R.H: relative humidity
SDBS: sodium dodecylbenzene sulfonate
SEM: Scanning Electron Microscopy
SILMs: supported ionic liquid membranes
SPEEK: sulfonated poly(ether ether ketone)
SWCNT: single-walled carbon nanotube
TEA: techno-economic analysis
TRL: technology readiness level
TPC: total plant cost
TPD: tonne per day
UB: University at Buffalo, The State University of New York
vol%: percentage by volume
wt%: percentage by weight
XPS: X-ray photoelectron spectroscopy

END OF REPORT